Paleoceanography and Paleoclimatology

RESEARCH ARTICLE
10.1029/2020PA003925

Special Section:
The Miocene: The Future of the Past

Decreasing Atmospheric CO_2 During the Late Miocene Cooling

Thomas Tanner[1], Iván Hernández-Almeida[1], Anna Joy Drury[2], José Guitián[1], and Heather Stoll[1]

[1]Geological Institute, ETH Zurich, Zurich, Switzerland, [2]Department of Earth Science, University College London, London, UK

Key Points:
- The alkenone-based proxy for reconstructing atmospheric CO_2 levels shows a coupling of temperature and CO_2 during the late Miocene cooling
- Reconstruction of sea-water $\delta^{18}O$ shows a freshening and northward shift of the Antarctic Polar Front during the late Miocene cooling
- Frontal movements and biological pump in the Southern Ocean may have driven CO_2 drawdown and storage in deep ocean

Supporting Information:
- Supporting Information S1

Correspondence to:
T. Tanner,
thomas.tanner@erdw.ethz.ch

Citation:
Tanner, T., Hernández-Almeida, I., Drury, A. J., Guitián, J., & Stoll, H. (2020). Decreasing atmospheric CO_2 during the late Miocene cooling. *Paleoceanography and Paleoclimatology*, *35*, e2020PA003925. https://doi.org/10.1029/2020PA003925

Received 18 MAR 2020
Accepted 2 NOV 2020
Accepted article online 10 DEC 2020

Abstract A pronounced late Miocene cooling (LMC) from ~7 to 5.7 Ma has been documented in extratropical and tropical sea surface temperature records, but to date, available proxy evidence has not revealed a significant pCO_2 decline over this event. Here, we provide a new, high-resolution pCO_2 proxy record over the LMC based on alkenone carbon isotopic fractionation (ε_p) measured in sediments from the South Atlantic at Ocean Drilling Program (ODP) Site 1088. We apply a recent proxy calibration derived from a compilation of laboratory cultures, which more accurately reflects the proxy sensitivity to pCO_2 changes during late Quaternary glacial-interglacial cycles, together with new micropaleontological proxies to reconstruct past variations in algal growth rate, an important secondary influence on the ε_p. Our resulting pCO_2 record suggests an approximately twofold to threefold decline over the LMC and confirms a strong coupling between climate and pCO_2 through the late Miocene. Within this long-term trend are pCO_2 variations on sub-myr timescales that may reflect 400-kyr long-eccentricity cycles, in which pCO_2 minima coincide with several orbital-scale maxima in published high-resolution benthic $\delta^{18}O$ records. These may correspond to ephemeral glaciations, potentially in the Northern Hemisphere. Our temperature and planktonic $\delta^{18}O$ records from Site 1088 are consistent with substantial equatorward movement of Southern Ocean frontal systems during the LMC. This suggests that potential feedbacks between cooling, ocean circulation and deep ocean CO_2 storage may warrant further investigation during the LMC.

1. Introduction

The late Miocene offers the opportunity to assess the sensitivity of the Earth's climate to orbital forcing and to changing boundary conditions, such as ice volume and greenhouse gas concentrations, on a sometimes warmer-than-modern Earth (Holbourn et al., 2018). It was a time period where significant global changes in climate have occurred. Starting about seven million years ago, both hemispheres witnessed synchronous cooling and large areas of the continents experienced drying (Schuster et al., 2006). Recent globally distributed sea surface temperature (SST) reconstructions also show substantial and coherent long-term, large-magnitude ocean cooling starting at around the same time (Herbert et al., 2016). Large-scale cooling and aridification during the late Miocene could have initiated a positive feedback loop with possible growth of ice sheets and deserts leading to a significant increase in continental albedo and further decrease of global temperatures.

During the late Miocene, the Antarctic ice sheets were already relatively stable, while ice sheets in the Northern Hemisphere were likely small and ephemeral, prior to the onset of permanent Arctic glaciation around 3.2 Ma (Holbourn et al., 2018; Zachos et al., 2001). Strong obliquity cycles appear in benthic ^{18}O records at 7.7 Ma supporting high-latitude forcing and increased Northern Hemisphere glacial activity (Drury et al., 2017). A long-term trend toward heavier benthic $\delta^{18}O$ maxima in the Ocean Drilling Program (ODP) Site 1146 record in the South China Sea started around 7 Ma and is punctuated by orbital-scale events of globally traceable benthic $\delta^{18}O$ excursions up to 3‰. These periodic benthic $\delta^{18}O$ maxima are in the range of late Pliocene values and transitional values between peak Holocene and glacial levels at the same location, therefore indicating times of such ephemeral Northern Hemisphere glaciation (Holbourn et al., 2018).

Carbon isotopes in soils also show important global ecological changes during the late Miocene and the early Pliocene with a shift in dominance from C3 to C4 plants between 4 and 8 Ma in Asia (Cerling et al., 1997).

However, considering that the large-magnitude cooling would be unfavorable for the expansion of C4 plants, their appearance in the geological record is best explained by an environment of declining atmospheric CO_2 levels (Cerling et al., 1997; Herbert et al., 2016). Furthermore, a large divergence between the carbon isotopic compositions of small versus large coccoliths arose during the same time period (Bolton & Stoll, 2013). It is hypothesized that coccolithophores at low $[CO_2]_{aq}$ increase their demand of HCO_3^- at the site of photosynthesis by diminishing the allocation of HCO_3^- to calcification, which is most pronounced in larger cells and may explain the divergence in $\delta^{13}C$. The findings of these so-called "vital effects" further strengthen the theory of declining pCO_2 during the late Miocene.

Although the indirect evidence from these proxies suggests change in pCO_2 during this interval, the exact role of CO_2 in the evolution of the global climate across the late Miocene is still under debate, mostly because of the low resolution of existing direct pCO_2 reconstructions (Sosdian et al., 2018). Consequently, the late Miocene was long thought of a period with a climate decoupled from atmospheric pCO_2 (Pagani et al., 2005) and to date, most reconstructions support a decoupling between pCO_2 and climate during the Miocene and Late Pliocene (LaRiviere et al., 2012).

In this study, we reconstruct atmospheric pCO_2 between 8 and 4.5 Ma at the highest (average 125 kyr, between 5.5 and 7 Ma at ~55 kyr) resolution to date, using the carbon isotope fractionation during photosynthesis measured in alkenones (ε_p) in a sediment core in the South Atlantic. ε_p is a widely used pCO_2 proxy sensitive to dissolved CO_2 (Pagani, 2014) and other physiological parameters such as cell growth rate and size. We employ a recent recalibration of the ε_p pCO_2 proxy based on laboratory culture studies (Stoll et al., 2019) and estimate with independent proxies the effect of the physiological parameters in coccolithophores which have been shown to be important for ε_p. In particular, we evaluate the changing ocean surface hydrological situation, including stratification and frontal movements, over this time interval to improve our understanding of potential growth rate variations in coccolithophores. Our result yields a high-resolution pCO_2 reconstruction defining a clear decline coincident with the late Miocene cooling (LMC).

2. Site Locations and Oceanographic Setting

ODP Site 1088 (41.13°S, 13.6°E) was drilled during ODP Leg 177, in the southeastern South Atlantic, on the northeastern limit of the Agulhas ridge, at a water depth of 2,082 m, well above the modern lysocline in this region and therefore with excellent carbonate preservation. The studied samples were recovered from Hole 1088B using advanced piston coring (APC), between 39 and 93 meters composite depth (mcd) and belong to a single lithostratigraphic unit dominated by nannofossil ooze with variable amounts of foraminifera. Details about the sedimentological and physical properties of Site 1088 can be found in the Leg 177 Initial Reports (Gersonde et al., 1999). ODP Site 1090 (42.9°S, 8.8°E) was drilled during the same ODP Leg 1077 and is very close to the position of Site 1088, at a water depth of 3,700 m.

Today, Site 1088 is located south of the Subtropical Front (STF) in the Southern Ocean and north of the Subantarctic front (SAF). The area between these two fronts is defined as the Subantarctic Zone (SAZ) and is characterized by a large temperature gradient, from 15°C north of the STF to 8°C south of the SAF (Figure 1). Modern SST varies seasonally between 10°C and 15°C, with an annual mean of 13–14°C, and salinity is relatively constant, around 34‰, while $\delta^{18}O_{sw}$ is 0.16‰. Cold and fresher subantarctic surface waters with negative $\delta^{18}O_{sw}$ values can reach Site 1088 by cross-frontal northward transport (De Ruijter et al., 1999) (Figure 1). Dissolved phosphate ($[PO_4^{3-}]$) in surface waters is 0.75 μM. Coccolithophores calcify mainly during summer (December to February) in middle to high latitudes in the Southern Hemisphere (Hopkins et al., 2015), and average modern growth rates for the summer months based on model parametrizations (Krumhardt et al., 2017) are 0.9 day^{-1} (divisions/day) at Site 1088. Paleoceanographic records at Site 1088 and 1090 during the Late and Middle Pleistocene have shown that the position of the SAF has shifted repeatedly at orbital and suborbital timescales, bringing colder, fresher, and nutrient-rich waters to the position of Site 1088 during episodes of glacial expansion (Kemp et al., 2010). The paleogeography of Site 1088 (Table S4 in Herbert et al., 2016) during the observed time interval is very similar to today and has not significantly moved. Around 8 Ma, the site was roughly 1.03° south and 1.99° west of today's location. Based on a calculation of pre-industrial $[CO_2]_{aq}$, we additionally assume the site is near equilibrium with the atmosphere (Figure S1 in the supporting information).

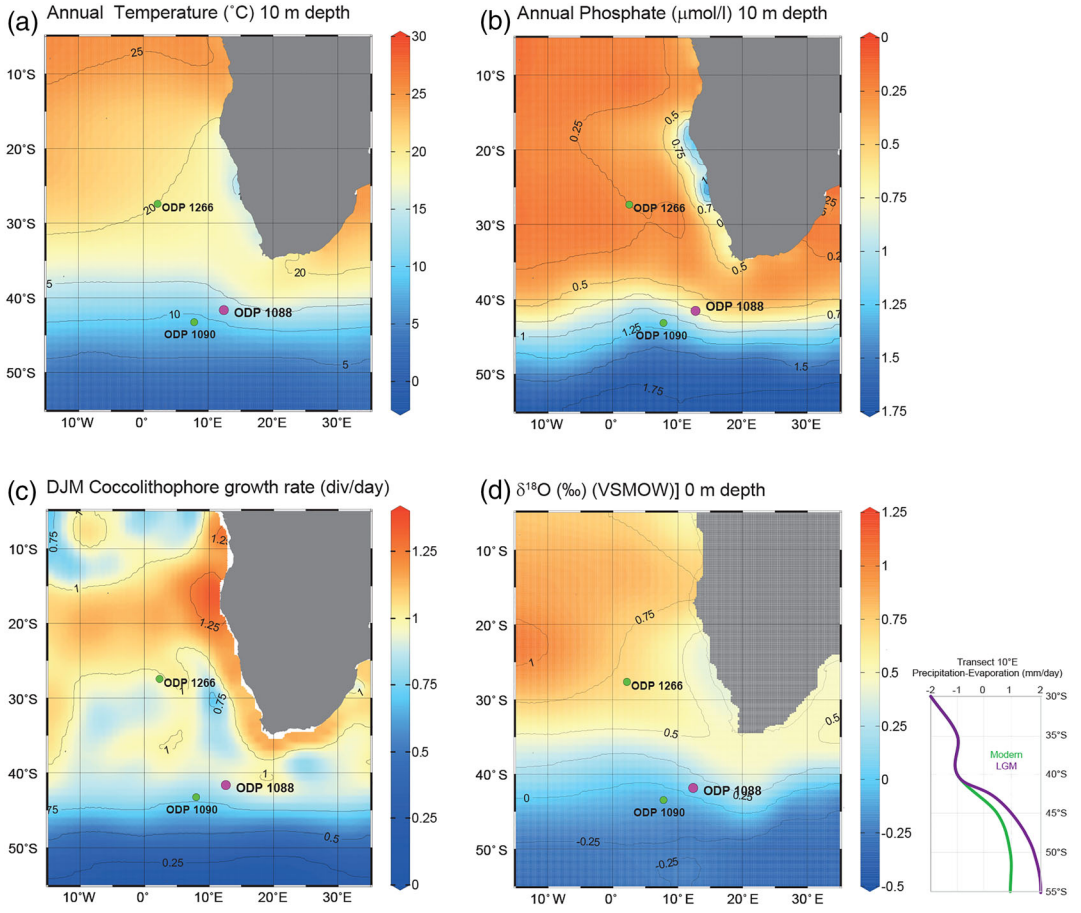

Figure 1. Overview of the modern ocean setting. Symbols show the locations of ODP Expedition 177 Sites 1088 and 1090 and IODP Site 1266. Modern-day data are highlighted in four panels: (a) Annual temperature (Locarnini et al., 2013) and (b) annual phosphate (Garcia et al., 2013) were extracted from gridded World Ocean Atlas 2013 (WOA13) using Ocean Data View (ODV), (c) Southern Hemisphere summer months (DJM) coccolithophore growth rate after Krumhardt et al. (2017), and (d) oxygen isotope composition of surface waters after LeGrande and Schmidt (2006); small panel shows the modeled precipitation-evaporation for the pre-industrial control and LGM from the BRIDGE simulations (Valdes et al., 2017).

To provide context for the Miocene proxy interpretation, several samples of Pleistocene age were also examined. Unfortunately, Late Pleistocene sediments could not be sampled from Site 1088 as the core is fully depleted; for this location we have relied on published SST and foraminiferal isotope data from Site 1090 (SST from Martínez-Garcia et al., 2010, and $\delta^{18}O$ from Hodell et al., 2003); incorporated results are shown in Table S1. We have conducted new analyses from Site 1266, which was recovered during ODP Leg 208 (28°31.97′S, 2°46.77′E) on the southern flank of Walvis Ridge, at a water depth of 3,806 m, also above the lysocline during the Cenozoic (Zachos et al., 2004). At 1266, Late Pleistocene sediments are characterized by high content in well-preserved nannofossil and foraminifera. Site 1266 is currently situated in the subtropical gyre, with modern SST in the range of 20°C, average annual $[PO_4^{3-}]$ of 0.23 µM, and more saline and higher $\delta^{18}O_{sw}$ surface waters than Site 1088. As we discuss in section 5.1, the modern surface hydrography of 1266 may be analogous to that of Site 1088 during times in the late Miocene.

3. Methods

3.1. Organic Geochemistry

The total lipid extract (TLE) was obtained from 25–35 g of freeze-dried sediment, using a Dionex 350 accelerated solvent extractor from Thermo, with a 5:1 ratio of dichloromethane to methanol (CH_2Cl_2/MeOH) extraction solvent in four static cycles at 100°C. The TLE was saponified by adding a 2-ml mixture 0.5-M

KOH in 95:5 MeOH/H_2O and heating it for 2 hr at 75°C. The neutral fraction was obtained and eluted through silica gel columns for small-scale separation of, aliphatic hydrocarbons using 4 ml of Hexane, ketone fraction with 4 ml of CH_2Cl_2, and a polar fraction using 4 ml of MeOH.

The ketone fraction, containing the alkenones, was dried under an N_2 stream and dissolved in toluene to be injected for quantification at ETH Zurich. Samples were analyzed on a Thermo Scientific Trace 1310 Gas Chromatograph (GC) equipped with an Agilent non-polar (60 m × 0.25 mm × 0.25 μm) capillary column (VF-200ms) and 5-m guard column with 2-ml/min He as carrier gas flow. Samples were injected into a programmable temperature vaporization (PTV) inlet and quantified by flame ionization detection (FID). GC oven held initial temperature of 120°C for 1 min, ramped first by a temperature increase of 40°C/min to 200°C, then followed by 5°C/min to 300°C, and held isothermal for 15 min. Finally, it was ramped 2°C/min to 320°C. For each sample, a known amount of *n*-alkanes C_{38} and C_{40} was added as internal standard. $U^{k'}_{37}$ ratio was estimated directly from the FID after the abundance of the C_{37} diunsaturated and triunsaturated ketones. Lab-sample replicates and in-house alkenone standard were injected every sequence to determine instrument drift and to guarantee long-term validation giving a precision of 0.025 $U^{k'}_{37}$ units. Alkenone-derived SST was calculated from $U^{k'}_{37}$ using the global calibration from Müller et al. (1998), the same calibration on which previous published SST from Site 1088 were presented (Herbert et al., 2016).

Carbon isotopic compositions of $C_{37:2}$ alkenones were measured on a Thermo Scientific Delta V mass spectrometer interfaced with a Thermo Scientific Trace 1310 GC (irMS) at ETH Zurich. GC was equipped with an Agilent non-polar capillary column (VF-200ms) using a 2-ml/min He as carrier gas flow. Initial GC temperature was set at 90°C and ramped to 250°C at 25°/min, increased to 305°C at 1°/min, and finally increased to 320°C at 10°/min to be held isothermally for 7 min. Replicates, in-house alkenone standard, and known isotopic mixtures A5 and B4 (supplied by Arndt Schimmelmann, University of Indiana) were injected at every sequence to determine the analytical accuracy of the measurement and an uncertainty of 0.4‰ is reported. Carbon isotopes are reported relative to the Vienna PeeDee Belemnite (VPDB) standard.

3.2. Inorganic Geochemistry

Previously freeze-dried and organic extracted bulk sediment was sieved with deionized water through a 150-μm sieve and oven dried overnight at 50°C. Several planktonic foraminifera species (*Globigerina bulloides*, *Neogloboquadrina pachyderma sinistral [sin.]*, and *Globoconella spp*.) and the benthic foraminifera genus *Cibicidoides spp*. were picked in Miocene samples from Site 1088. The species picked belonging to the subgenus *Globoconella* were mainly *Globoconella conoidea* (until 55 mcd) and *Globoconella conomiozea* (below 55 mcd). Species from *Globoconella* subgenus have been proposed to represent conditions in the thermocline since the early Miocene (Norris et al., 1994). For the Last Interglacial (MIS5, 125 ka) and Last Glacial Maximum (LGM, 20 ka) samples from Site 1266, the species *Globigerina inflata*, *Globigerinoides ruber*, and *Globorotalia truncatulinoides* were picked. Typically, 10–15 planktonic specimen and 5 benthic specimen larger than 150 μm were picked per sample. Foraminifera were crushed, rinsed twice with deionized water and once with MeOH, and dried overnight at 50°C. Samples were analyzed at ETH Zurich on a GAS BENCH II system coupled to a Delta V Plus irMS (Thermo Scientific) following procedures described by Breitenbach and Bernasconi (2011). Analytical precision after system calibration by two in-house standards and international standards NBS-19 and NBS-18 was 0.07‰ for both stable isotopes. Values are reported relative to the VPDB standard. Measurement replicates yielded a mean difference for oxygen and carbon isotopes of 0.04‰. The equation used to reconstruct $\delta^{18}O_{sw}$ from paired alkenone-SST-$\delta^{18}O_c$ measurements on *N. pachyderma sin*. and *G. bulloides* is that of Shackleton (1974) ($\delta^{18}O_{sw} = \delta^{18}O_c + 0.27 - (4.38 - (4.382–4 \times 0.1(16.9 - T))^{1/2})/(0.1 \times 2)$). We did not account for any "vital effects" in $\delta^{18}O_c$ since we simply wanted to observe temporal changes and trends, which should not be affected if the "vital effects" stayed constant over time.

3.3. Coccolith Size Reconstruction

The coccolith size used for pCO_2 calculations was estimated in two steps. First, the calcareous nannofossil biostratigraphy at Site 1088 (Marino & Flores, 2002) contains semiquantitative abundance data on the alkenone producing coccolithophorid *Reticulofenestra pseudoumbilicus* on a scale of numerical representation (0 = *absent*, 0.2 = *very rare*, 1 = *rare*, 2 = *few*, 6 = *common*, 8 = *abundant*, and 10 = *very abundant*). Data from smear slides cover the analyzed depth interval of this study, and a weighted size is interpolated for

each sample (Figure S2). Therefore, a mean size for each of the four published size categories (<3 μm = 2 μm, 3–5 μm = 4 μm, 5–7 μm = 6 μm, and >7 μm = 8 μm) was chosen, multiplied with the numerical representation for each size (*a*, *b*, *c*, and *d*) and finally divided by the total numerical representation of the size composition, illustrated with the following equation:

$$weighted\ size = \frac{2a + 4b + 6c + 8d}{a + b + c + d} \quad (1)$$

Second, a fully quantitative estimation of the mean size of *Reticulofenestra pseudoumbilicus* from a subset of five samples was carried out using polarized light microscopy and the C-Calcita software (Fuertes et al., 2014). Those five samples represent the whole range of semiquantitative size (small-mid-large), and they are used to accurately quantify the size classes from assemblage counts. The difference between weighted coccolith size and quantitative size is almost negligible, with the semiquantitative size underestimating at the smaller and overestimating at the larger end of the size spectrum (Figure S3). Therefore, the reported coccolith size values are the weighted sizes corrected with this secondary regression.

3.4. Calculation of ε_p

The isotopic fractionation (ε_p) during photosynthetic fixation of carbon between $[CO_2]_{aq}$ and algal biomass is calculated using the following equation originally described by Freeman and Hayes (1992):

$$\varepsilon_p = \left(\frac{\delta^{13}C_{[CO2]aq} + 1000}{\delta^{13}C_{org} + 1000} - 1\right) * 1000 \quad (2)$$

The isotopic difference between phytoplankton biomass $\delta^{13}C_{org}$ and $\delta^{13}C_{37:2}$ is 4.2‰ (Popp et al., 1998) and takes into account that lipids are lighter than the total cell organic carbon (Jasper et al., 1994), which is the value expressed in $\delta^{13}C_{org}$. It is applied as follows:

$$\delta^{13}C_{org} = \delta^{13}C_{37:2} + 4.2‰ * \left(1 + \frac{\delta^{13}C_{37:2}}{1000}\right) \quad (3)$$

The values for $\delta^{13}C_{[CO2]aq}$ are derived using the initial $\delta^{13}C$ values for *N. pachyderma sin.* as a first assumption of $\delta^{13}C_{DIC}$. The mean offset between mixed layer depth $\delta^{13}C_{DIC}$ and $\delta^{13}C_{pachyderma}$ in sediment traps in the North Atlantic (latitude) is 0.81‰ (Jonkers et al., 2013). As there is no equivalent at similar latitudes in the South Atlantic, we add 0.81‰ to the downcore $\delta^{13}C_{pachyderma}$ at Site 1088 to correct the vital effect in $\delta^{13}C$. Calculation of DIC value into an isotopic CO_2 signal, which is lighter than DIC, and depends on temperature (derived from $U^{k'}_{37}$; in kelvins) and pH (which is neglected) follows the equation from Rau et al. (1996) based on Mook et al. (1974):

$$\delta^{13}C_{[CO2]aq} = \delta^{13}C_{DIC} + 23.644 - \left(\frac{9701.5}{T}\right) \quad (4)$$

To carefully include and propagate the uncertainties of each parameter introduced, whether it is for ε_p or any subsequent calculation, a full Monte Carlo simulation (n = 10,000) was conducted. The input parameters (Table S5) were randomly sampled within 2 standard deviations (s.d.) of the mean of the following uncertainties: ±1.5°C for temperature based on the reported calibration error by Müller et al. (1998); ±0.1‰ for foraminiferal calcite $\delta^{13}C$ and the standard error of the mean (between ±0.05 and ±0.43‰) for alkenone $\delta^{13}C$, conservative error estimates based on replicate runs; ±0.13 μm for the cell size based on the regression uncertainty between semiquantitative and quantitative size; ±10% for light and ±0.1 μM for phosphate, based on the mean standard error of the sigmoidal model regression. This approach is in agreement with recent publications in the field (e.g., Badger et al., 2019; Y. G. Zhang, Henderiks, et al., 2020), and all the error bars in all relevant figures are 1 s.d.

3.5. Age Model Composite Core Images, Color Profiles, and Magnetic Susceptibility Data

Composite core images for Hole 1088B were generated by cutting individual core sections from core table photos (downloaded from JANUS: http://www-odp.tamu.edu/database/). Each section image was then

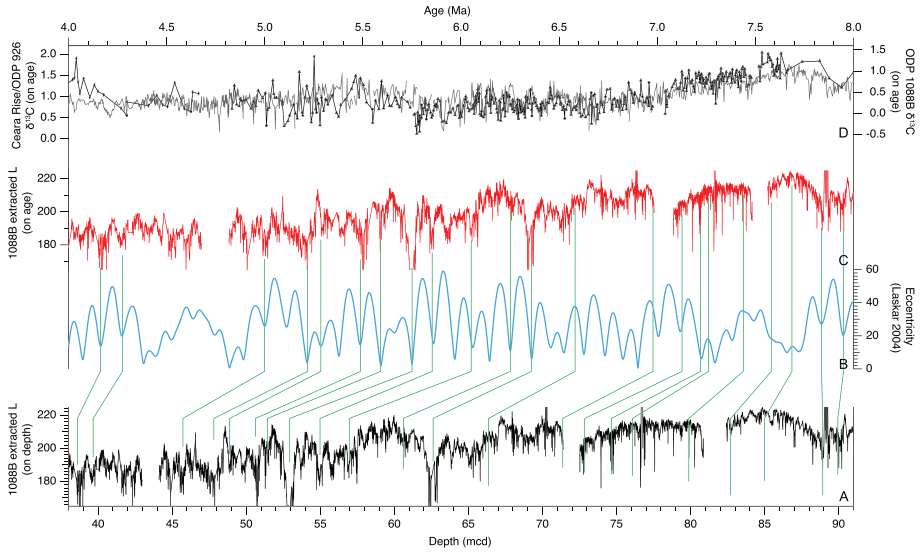

Figure 2. Minimal tuning applied to Hole 1088B, with (a) the extracted L data on depth, (b) the eccentricity tuning target from Laskar et al. (2004), (c) the extracted L data converted to age, and (d) the benthic $\delta^{13}C$ data from Hole 1088B ((Billups, 2002; Billups et al., 2008; Hodell et al., 2003; Hodell & Venz-Curtis, 2006; this study) compared to the benthic $\delta^{13}C$ data from the equatorial Atlantic Ceara Rise stack/ODP Site 926 (Drury et al., 2017; Shackleton & Hall, 1997; Wilkens et al., 2017).

compiled and scaled to the shipboard mcd using the Includes_Core_Table_Photos functions within Code for Ocean Drilling Data (CODD v1; Wilkens et al., 2017). To account for the single-point lighting source used in core table photos, a lighting correction was also applied.

As shipboard color reflectance data were not collected at Site 1088, core color information (hue, saturation, lightness, red, green, and blue) was extracted every mm from the composite core images using the CODD "CreateHoleCoreImageProfiles" function. The extracted lightness (L) showed the clearest variability and was chosen to approximate Lstar data. The top 4 cm of each section was excluded from the L profile to remove a lighting artifact at section ends. To account for core heterogeneity, the L data were then despiked using the CODD "Median_DeSpike" function (despiked data over 2 s.d. from the median within a 400-point/0.4-m window) and then smoothed using an 11-point binomial smoothing. All extracted data are provided in supporting information Table S1.

The composite core images from Hole 1088B show clear evidence for core disturbance at the top of most cores (supporting information Table S2). These intervals were excluded from the extracted lightness and shipboard magnetic susceptibility (MS) records. The shipboard MS data were also despiked using the "Median_DeSpike" function (despiked data over 2 s.d. from the median within a 40 point/0.4 m window; supporting information Table S3).

4. Results

4.1. Astrochronology

The composite core images, extracted L data and shipboard MS data show 2.5- to 3- and 8.5- to 9-m cycles, with intervals where 0.8- to 1-m cycles are present (Figure 2). Based on biostratigraphic age constraints from Marino and Flores (2002), updated to Neogene GTS 2012 (Hilgen et al., 2012), these cycles likely relate to short- and long-term eccentricity, with occasional obliquity influences. The MS and extracted L are approximately antiphase to each other. The high-resolution extracted L data have especially well-expressed cycles, with the highest-amplitude variability coinciding with the lowest overall L values. Around 38–40 mcd there are two distinct, high-amplitude minima in L, surrounded by progressively lower amplitude cycles, all approximately 110 kyr in duration. These high-amplitude cycles are very well expressed and likely occur during a 405-kyr eccentricity maximum when the short-term eccentricity cycles are strong.

Therefore, the lowest absolute L values occur during 405-kyr maxima. In the Pleistocene, the extracted L data have an inverse relationship with the benthic $\delta^{18}O$ data, with L maxima coinciding with benthic $\delta^{18}O$ minima. Based on the Pleistocene age control provided by Hodell et al. (2003), the extracted L data are in phase with the ~110-kyr eccentricity cycles. Although the available benthic $\delta^{18}O$ is too low resolution to confirm whether the Pleistocene phase relationships between extracted L, benthic $\delta^{18}O$ and eccentricity are also valid for the late Miocene and Pliocene, we assume that L maxima are in phase with short-term ~110-kyr eccentricity maxima.

An astrochronology for Hole 1088B was generated between 4.2 and 7.9 Ma (38–90 mcd; Figure 2), using 24 minimal tie points between L maxima and ~110-kyr eccentricity maxima (Ecc; Laskar et al., 2004). The amplitude modulation in the data broadly follows the amplitude modulation of eccentricity. Eccentricity is exceptionally poorly expressed in the L data during the 2.4-Myr eccentricity minima (4.4–4.8 and 7.3–7.7 Ma), and as such, the astrochronology is less secure in these intervals. The overall robustness of the astrochronology is constrained by the generally good agreement between the benthic foraminiferal $\delta^{13}C$ data from ODP Site 1088B (Billups, 2002; Billups et al., 2008; Hodell et al., 2003; Hodell & Venz-Curtis, 2006; this study) and equatorial Atlantic Ceara Rise/ODP Site 926 (Drury et al., 2017; Shackleton & Hall, 1997; Wilkens et al., 2017). The equatorial-south Atlantic benthic $\delta^{13}C$ correlation is particularly good across the late Miocene carbon isotope shift (LMCIS), which supports the accuracy of the astrochronology even though the amplitude in the L data in this interval is somewhat suppressed.

4.2. Alkenone Abundance and SST Reconstruction

The accumulation rate of alkenones ($C_{37}AR$, in ng/cm^2/kyr) is calculated using the amount of alkenones (ng/g) in the dry bulk sediment multiplied by the mass accumulation rate (MAR, in g/cm^2/kyr). Since the sediment was not powdered in order to permit separation of intact foraminifera post extraction and no extraction standard was used, this metric must only be used as a qualitative trend and should not be compared with that of other publications. MAR is calculated by the multiplication of linear sedimentation rate (LSR) with the dry bulk density (DBD, from Diester-Haass et al., 2005). With the new age model, LSR changes with respect to previous publications. MAR and $C_{37}AR$ can be seen in Figure S2. The MAR steadily decreases during the LMC from roughly 3 to 1 g/cm^2/kyr and the $C_{37}AR$ increases from roughly 100 to almost 400 ng/cm^2/kyr.

The reconstructed SST (Figure 3d) produces the same trend and, in large, similar values as previously published for Site 1088B by Herbert et al. (2016). The new measured samples reflect the long-term cooling trend over the LMC with temperatures decreasing 5–6°C from 20°C around 7.5 Ma to 14.5°C around 5.7 Ma. This long-term cooling abruptly ended with a 5–6°C increase within less than 130 kyr (red shaded interval in Figure 3).

4.3. Stable Isotopes

At Site 1088, the three planktonic foraminifera species show broadly similar trends in $\delta^{18}O$ (Figure 3), with differences in the absolute values as a function of their habitat depth. *G. bulloides* and *N. pachyderma sin*. show very similar values for most of the record, except for a sample older than 7.5 Ma in which they diverge (almost 0.5‰). *Globoconella spp*. shows heavier values than the other two species with an average offset of 0.6‰ to *N. pachyderma sin*., indicating a deeper habitat.

Another important observation from this data set is that the time period of the temperature change from 15°C to 20.5°C around 5.7 Ma coincides with very similar $\delta^{18}O$ values for all three species. The samples representing the points for 15°C and 20.5°C are even happening at a time of 0‰ difference between the deep and intermediate dwelling species. $\delta^{18}O$ values for the benthic species *Cibicidoides spp*. and the planktonic species *G. bulloides* are displayed over existing data from Billups et al. (2008). The minor differences among the two data sources for the planktonic $\delta^{18}O$ are probably caused by measurement of different sizes since Billups et al. (2008) used the larger 250- to 355-μm fraction.

The planktonic foraminiferal carbon isotope values ($\delta^{13}C$) for *N. pachyderma sin*. (Figure 4b) decrease by about 1‰ during the time of the LMCIS (from 7.5 to 6.7 Ma). The LMCIS has been shown to be a globally synchronous event in benthic and planktic foraminifera (Drury et al., 2017), indicating a change in $\delta^{13}C$ of oceanic DIC driven by changes in ocean circulation (Hodell & Venz-Curtis, 2006) rather than changes

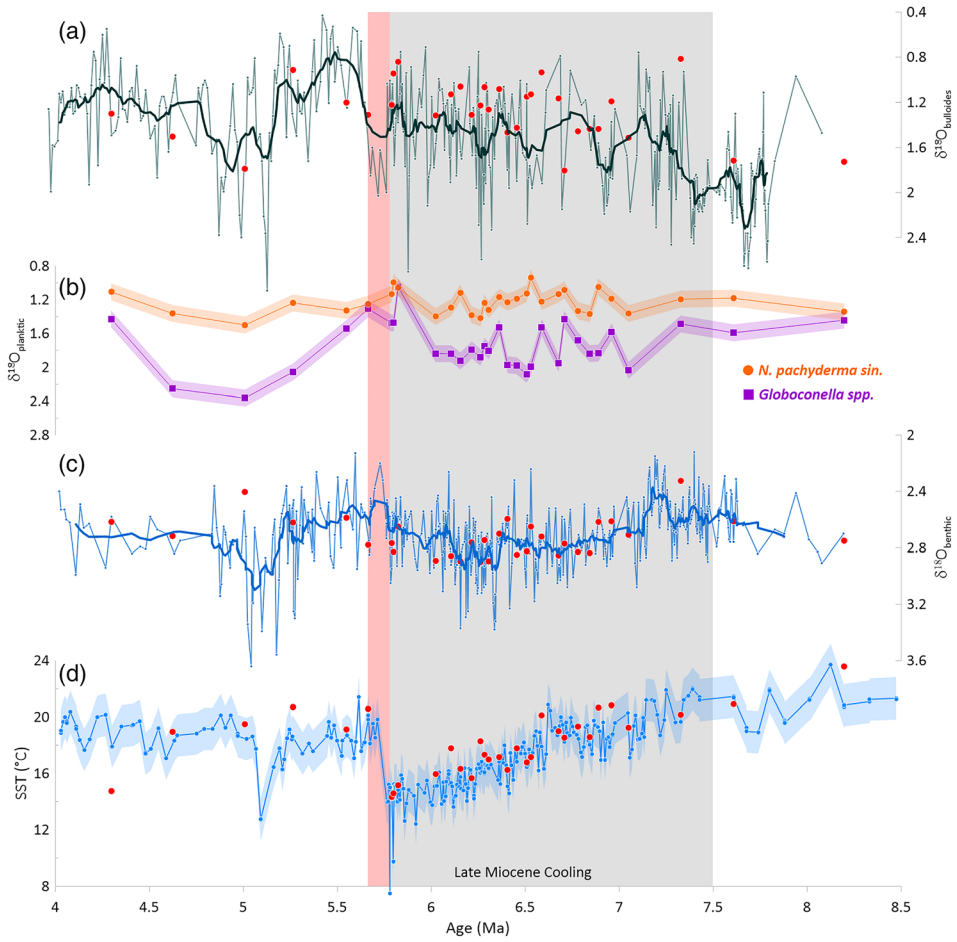

Figure 3. ODP Site 1088 (a) $\delta^{18}O$ of planktonic species *G. bulloides*. Existing data from Billups et al. (2008) in dark green with an 11-point running average in bold (250- to 355-μm size fraction). (b) $\delta^{18}O$ of *N. pachyderma sin*. in orange and *Globoconella spp*. in purple. Shadings represent a ±0.1‰ error estimation. (c) $\delta^{18}O$ of the benthic species *Cibicidoides spp*. existing data from Billups and Schrag (2002) and Billups et al. (2008) in dark blue with an 11-point running average in bold (250- to 355-μm size fraction). (d) Alkenone-based sea surface temperatures from Herbert et al. (2016) in blue with a ±1.5°C error shading. Red dots in all graphs show the new measurements carried out during this study, and all this is updated to the new age model. The red shaded bar indicates the abrupt end of the LMC.

in productivity (Drury et al., 2018). *G. bulloides* shows an unknown disequilibrium process in $\delta^{13}C_{bulloides}$ in the Southern Ocean (>40°S) (Prasanna et al., 2016), which is why the carbon isotopes of *N. pachyderma sin*. are used for the following calculations.

The values from the alkenone carbon isotope record ($\delta^{13}C_{37:2}$) range from −22.90‰ to −24.64‰ (Figure 4a). Large changes of up to 1.3‰ from one to the next sample are observed in the part older than 6.5 Ma; the younger time interval shows less variation. There is also no clear overall trend visible. The final values for ε_p (Figure 4c) are between 10.88‰ and 12.79‰ and show similar fluctuations as the $\delta^{13}C_{37:2}$. Overall, a small decreasing trend is noticeable.

4.4. Late Pleistocene Proxies in ODP Site 1266

In the four samples from Site 1266, representing glacial and interglacial times, *N. pachyderma sin*. is not present. Therefore, the DIC estimations for the ε_p calculations at 1266 are based on the species *G. inflata*. Based on core-top observations, the $\delta^{13}C$ offset between *G. inflata* and *N. pachyderma sin*. is −0.95‰ (Elderfield et al., 2002), which is added to $\delta^{13}C_{inflata}$ as correction to compare it with $\delta^{13}C_{pachyderma}$ records of Site

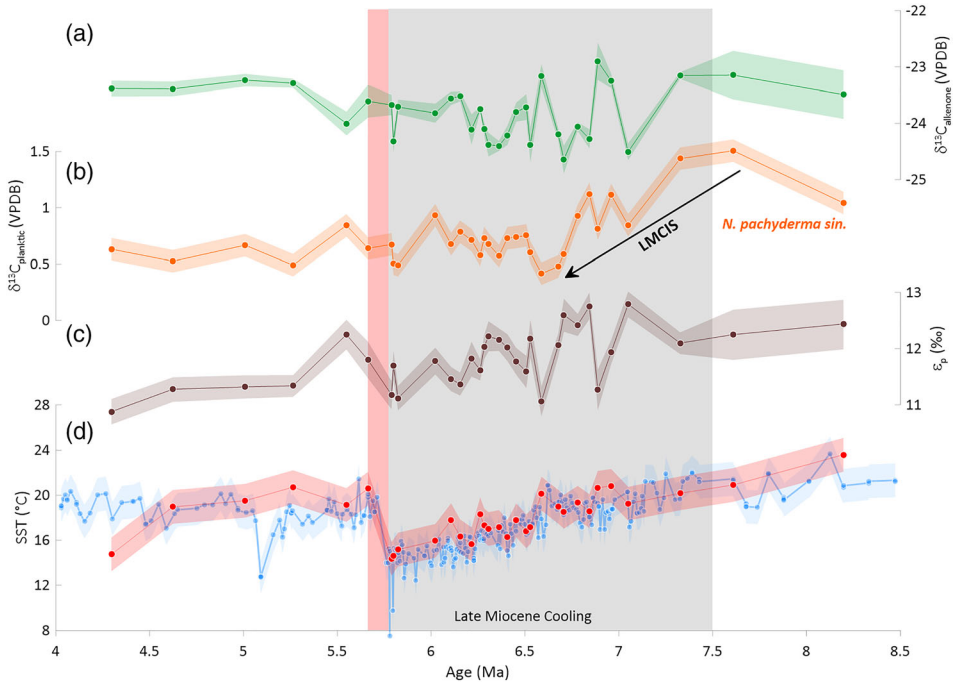

Figure 4. ODP Site 1088 (a) $\delta^{13}C$ of the organic matter of alkenone $C_{37:2}$ with green shading showing the standard error of the mean after multiple measurements. (b) $\delta^{13}C$ of the planktonic species *N. pachyderma sin*. with orange shading showing the ±0.1‰ error envelope. The black error indicates the timing of the late Miocene carbon isotope shift (LMCIS) between 7.5 and 6.7 Ma. (c) Resulting εp with brown shading showing the error propagated with the Monte Carlo simulation from $\delta^{13}C$ (alkenones and *N. pachyderma sin*.) and temperature. (d) Alkenone-based SST from Herbert et al. (2016) in blue with red dots indicating measurements from this study, both with a ±1.5°C error envelope. The red shaded bar indicates the abrupt end of the LMC.

1088. Additionally, the previously described correction of +0.81‰ for the vital effect between DIC and $\delta^{13}C_{pachyderma}$ is added and ε_p is calculated (Table S2). Additional measurements for $\delta^{18}O_{sw}$ at Site 1266 for the glacial and interglacial endmembers are shown in Table S1.

5. Discussion

5.1. Changing Surface Ocean Environment at Site 1088

5.1.1. Southern Ocean Frontal Movements

Changes of $\delta^{18}O$ in planktonic foraminifera may reflect changes in surface ocean temperature and/or the isotopic composition of surface seawater ($\delta^{18}O_{sw}$), which itself can reflect the local hydrological balance as well as ice-volume changes (Kucera, 2007). The gradual decrease of about 0.8‰ in $\delta^{18}O_{bulloides}$ during the late Miocene (Figure 3a) has been previously interpreted as a regional warming at Site 1088 of at most 3–4°C (Billups et al., 2008). However, alkenone SST reconstruction shows a clear cooling trend over the late Miocene (Herbert et al., 2016), discarding a temperature rise as the driver of the $\delta^{18}O$ decrease in *G. bulloides* at Site 1088. A large decrease in global ice volume (a sea level equivalent of 80 to 90 m at 0.09%/−10 m sea level; from Ravelo & Hillaire-Marcel, 2007) would be required to explain the decreasing trend in $\delta^{18}O$. However, New Jersey Margin sea level reconstructions do not show a large transgression during this time period (Miller et al., 2005) and melting Antarctic ice masses on such a magnitude during a time described as a global cooling seems unlikely. Crucially, the $\delta^{18}O$ of benthic foraminfera at Site 1088 stays relatively constant over this time interval (±0.3‰), with no evidence for a large decrease due to decreasing ice volume. This is in agreement with the long-term trends observed in late Miocene benthic $\delta^{18}O$ records from all major ocean basins (Drury et al., 2016, 2017; Hodell et al., 2001; Holbourn et al., 2018). Rather, the difference between benthic and planktic $\delta^{18}O$ increases by 0.8‰ over the LMC (Figure 5). We propose that $\delta^{18}O_c$ at Site 1088 evolved over the LMC due to a local surface freshening as hydrological fronts in the Southern Ocean moved equatorward and shifted the precipitation-evaporation (P-E) balance at the location.

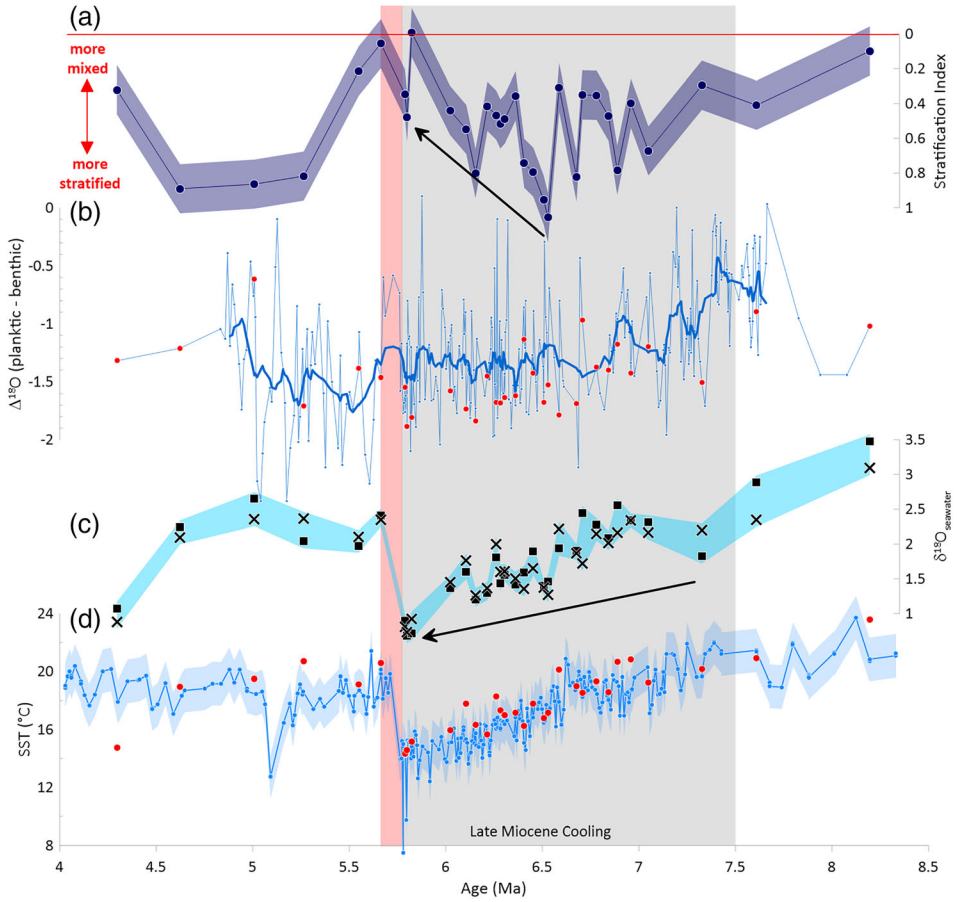

Figure 5. ODP Site 1088. (a) Stratification index "STRA" showing how the upper water column structure changed over time. The shaded error envelope (±0.14‰) reflects the propagated error of ±0.1‰ for $\delta^{18}O$ ($error = \sqrt{a^2 + b^2}$). The black arrow shows the gradual decrease in surface stratification. (b) Gradient between planktic (*G. bulloides*) and benthic (*Cibicidoides spp.*) foraminifera (Billups et al., 2008), red dots show the data from this study. (c) $\delta^{18}O_{sw}$ calculated using the two intermediate-dwelling species *G. bulloides*, marked with a square, and *N. pachyderma*, marked with a cross. The light blue shading is an expression of the overall observed trend based on two estimates of $\delta^{18}O_{sw}$. The black arrow indicates the gradual, long-term freshening at the location. (d) Alkenone-based SST from Herbert et al. (2016) in blue with a ±1.5°C error envelope. The red dots indicate the new measurements for 1088B from this study, and the red shaded bar indicates the abrupt end of the LMC.

If the temperature change reflected in the alkenone SST proxy is representative of the surface water temperature evolution experienced by *G. bulloides* or *N. pachyderma sin*. (e.g., reflect a similar depth habitat and season as the alkenone producers), then $\delta^{18}O_{sw}$ can be estimated from $\delta^{18}O_c$ according to the temperature calibration of calcite for that species (e.g., Shackleton, 1974). This approach yields a progressive decrease in $\delta^{18}O_{sw}$ of roughly 1.5‰ over the LMC (Figure 5c). The difference between benthic and planktic $\delta^{18}O$ exhibits a similar trend between 7.5 and 5.7 Ma but suggests a more modest 0.8‰ decline in planktic $\delta^{18}O$ relative to the benthic over the same time interval. Regardless of the contrast in estimated magnitude, both of these trends imply a relative decrease in local surface $\delta^{18}O_{sw}$ during the LMC.

In the modern ocean, there is progressive poleward depletion in $\delta^{18}O_{sw}$, with an ~1.5‰ range between 20°S and 55°S along the prime meridion in the South Atlantic (LeGrande & Schmidt, 2006) (Figure 1d). This poleward depletion reflects the transition from low P-E in the subtropical gyre to high P-E near the polar front, as well as a poleward progressive depletion in the $\delta^{18}O$ of precipitation due to lower temperature (Figure 1). We propose that equatorward movement of frontal positions during the LMC could cause a freshening leading to lighter, more depleted values in $\delta^{18}O_{sw}$ at the location of Site 1088. A shift of the Antarctic Polar Front (APF) toward the equator has been described to result from global cooling and can likely be linked to an onset of glaciation and feedbacks that lead to falling *p*CO2 (e.g., Toggweiler et al., 2006).

During the cooling from interglacial conditions to glacial maxima of the Late Pleistocene, an analogous equatorward movement of polar fronts in the region has been described. During the LGM, the APF and Subantartic Fronts (SAF) shifted equatorward by about 4–5° latitude (Gersonde et al., 2003) or potentially even more (APF up to 15°, SAF up to 9°, STF up to 7°) (see Kohfeld et al., 2013, and references therein). A glacial reduction of $\delta^{18}O_{sw}$ surface seawater at Site 1090 of 0.5‰ is estimated (from Hodell et al., 2003; Table S1) and fits the difference of water masses that are on either side of the APF today. Frontal movement during the LGM is also marked by an equatorward shift in the locus of maximum export production (Chase et al., 2003). The magnitude of cooling during the LMC, (5–6°C, estimated based on $U^{k'}_{37}$) is similar to or slightly larger than that observed for the last glacial-interglacial transition in the latitude band of 40–50°S in the present day SAZ (Kohfeld et al., 2013). Potentially, an equatorial shift in frontal positions with a comparable magnitude occurred between 7.5 and 5.7 Ma during the LMC.

The mechanism that describes the frontal movement during the LGM, which we take as an analog to the LMC, is a change in wind-driven circulation and precipitation patterns, associated with a steepening of the equator-to-pole temperature gradient and hence an intensification of the Hadley cell (Herbert et al., 2016; Holbourn et al., 2018). Such a scenario is also described in Kohfeld et al. (2013), where a stronger equator-to-pole thermal gradient could intensify the jet stream, leading to stronger Southern Hemisphere westerlies. Higher productivity in the SAZ may be sustained by enhanced wind-driven upwelling. A northward transport of cold polar and nutrient-rich waters by Ekman transport to the SAZ could explain an enrichment in nutrients at Site 1088.

In addition to equatorward frontal movement during the LMC, we also suggest that the APF and SAF were likely located poleward of their current interglacial position at the onset of the LMC. ODP Sites from Leg 114 (roughly 50°S, 28°W), which are today located within the Polar Front Zone, were proposed to be located north of the Polar Front during much of the late Miocene (Warnke et al., 1992). The late Miocene temperatures at Site 1088 prior to the onset of LMC are 10° or more warmer than modern SST (13–14°C), a contrast in climate state which may have been accompanied by further poleward frontal positions compared to the interglacial. Given these considerations, it is possible that the surface oceanographic conditions at Site 1088 in the late Miocene were more analogous to those of locations located in the modern-day subtropical gyre, such as the modern setting of Site 1266.

5.1.2. Stratification and Nutrient Supply

Today, deeper mixed layer depths are observed south of the SAZ (de Boyer Montégut et al., 2004), where vertical temperature gradients are less steep and surface ocean stratification less pronounced. Homogenization of upper water column properties by mixing is therefore not only more efficient in these polar regions in comparison to areas north of the SAZ but also leads to a greater abundance in nutrients via efficient recycling and redistribution. The gradient between intermediate (50–150 m) and deep living (below 200 m) planktonic foraminifera ($\Delta\delta^{18}O$ deep-interm.) in globally distributed core-top samples shows high correlation to $[PO_4^{3-}]$ in surface waters (10 m), which reflects the intensity of mixing in the water column (see Text S1). Downcore, we calculated the gradient (stratification index, "STRA") between intermediate and deep dwelling planktonic foraminifera using *N. pachyderma sin*. (Figure 5a), which at present today represents conditions in the intermediate water column (Jonkers et al., 2013), and *Globoconella spp*. As long as this gradient is predominantly driven by changes in the water column conditions at the typical foraminiferal depth habitats, and not changes in the depth habitat of one species relative to the other, then we expect this "STRA" gradient to track changes in nutrient supply to the surface ocean.

There is only indirect evidence for depth habitats of extinct planktonic foraminiferal species. All observations regarding this important issue result from oxygen isotope ratios of different species relative to each other (Keller, 1985; Norris et al., 1994). *Globoconella spp*. are assumed to have lived at the depth of the thermocline since the early Miocene based on the heavier $\delta^{18}O$ values (Keller, 1985) and are a typical species of the transitional zone, together with *G. bulloides* and *N. pachyderma*, that separates subtropical from subpolar waters (Kennett et al., 1985). *N. pachyderma sin*. is a typical polar to subpolar species in modern waters, while *G. bulloides* is a common dweller in the subpolar and temperate latitudes. In the Miocene, both species have been interpreted as having similar ecological habitat and dwelling in the mixed layer depth based on their $\delta^{18}O$ values (Kennett et al., 1985; Paulsen, 2005). The gradient between deep thermocline species, such as *Globoconella spp*., and mixed layer depth species, such as *N. pachyderma sin*. or *G. bulloides*, has been

previously interpreted in terms of water column stratification in records in the mid-latitude South Atlantic during the late Miocene (Matthews et al., 1980; Paulsen, 2005).

Over the LMC, the range of "STRA" at Site 1088 changes within 0‰ to 1‰ (Figure 5a), which is modest compared to the full range of 3‰ observed in the modern ocean. In the early part of the LMC, stratification is highly variable. From 6.5 Ma onward, there is a decreasing trend that parallels cooling of SST. Minimum stratification is observed between 5.5 and 5.9 Ma, including the time of the severest cooling and the first abrupt transition to warm temperatures at the end of the LMC. Lowest values of "STRA" are found today in well-mixed waters south of the polar front (Figure S4). The trend to lower stratification at Site 1088 happens around the same time for which Warnke et al. (1992) propose a significant Antarctic glacial expansion seen by the arrival of ice-rafted debris (IRDs) at ODP Sites 699 and 701 (50°S), possibly showing an expansion of Antarctic sea ice and a northward shift of the SAZ. We propose that the trend in "STRA" shows a deepening of the mixed layer depth, caused by either higher wind stress and/or by a reduction in density contrast across the upper water column. Both of these causes can be explained by a northward movement of the westerlies/SAZ, similar to the observations made in the previous section 5.1.1. This northward movement of the SAZ would in turn introduce nutrient-rich waters to the Site and potentially increase the biological productivity (e.g., Diester-Haass et al., 2005).

In fact, there is a resurgence of large *Reticuofenestra pseudoumbilicus* during the period of decreasing stratification (Figure S2). An inverse correlation between the abundance of larger coccoltihophores and water column stratification has been observed during the early Miocene in in the western subtropical South Atlantic, and it was proposed that more well-mixed surface waters with more nutrients could lead to an expansion of cell sizes (Henderiks & Pagani, 2007). This hypothesis is consistent with the observation that larger cell sizes have higher half saturation constants for nutrient acquisition and that nutrient abundance may favor expansion of cell sizes (Guitián et al., 2020). During this time interval there is also an increase in both the benthic foraminiferal accumulation rate (BFAR) (Diester-Haass et al., 2005) the C_{37}AR (Figure S2). Enhanced surface production may contribute to these increased accumulation rates, although changes in bottom water conditions are also likely to play a role.

5.2. Estimation of pCO_2 From Alkenone ε_p

5.2.1. Diffusive Versus Culture-Based Empirical Calibration Approaches

Traditionally, alkenone-based pCO_2 reconstructions were based on a diffusive model, recently reviewed by Pagani (2014). In the most widely used formulation (Jasper et al., 1994), a single coefficient, "*b*," was used to relate ε_p and CO_2 and encompasses all non-CO_2 effects on fractionation including growth rate, cell geometry, and other physiological factors. This simplified model assumes a theoretical hyperbolic relationship between ε_p and CO_2. However, recent evaluation of fractionation during laboratory experiments suggests that the empirical relationship between CO_2 and ε_p is logarithmic (Stoll et al., 2019), with ε_p less sensitive to CO_2 in the low CO_2 range (Badger et al., 2019) than previously inferred by the diffusive model. This is likely due to the operation of carbon concentrating mechanisms (CCMs). Based on culture data, a multilinear regression model was proposed in which ε_p is dependent on $[CO_2]_{aq}$, cell radius, growth rate (μ), and light (Stoll et al., 2019). This model incorporates the nonlinear response of ε_p to changes in $1/[CO_2]_{aq}$ which include empirical effects of CCMs on ε_p, as observed across culture experiments. The main advantage of this culture calibration is that it closely approximates the sensitivity of ε_p to CO_2 during Quaternary glacial-interglacial cycles as recorded by alkenones, in sites which are unlikely to have experienced significant changes in nutrient- or temperature-stimulated growth rates such as the tropical oligotrophic ocean (ODP Sites 925 and 999).

The drawback of such a model is that it is empirical, not a process-based physical model. Therefore, its applicability is best for settings most analogous to the culture conditions in which it was calibrated and the late Quaternary CO_2 oscillations in the tropical oceans where it was validated. However, the tropical oligotrophic sites are those of lowest $[CO_2]_{aq}$ are likely to feature the most intense reliance on CCMs and therefore a low sensitivity of ε_p to changes in $[CO_2]_{aq}$ (Stoll et al., 2019). From late Quaternary data alone—limited to a range of 180–280 ppm—it is not possible to ascertain whether this sensitivity of ε_p to $[CO_2]_{aq}$ may be higher in settings where $[CO_2]_{aq}$ limitation is less extreme. The culture calibration encompasses $[CO_2]_{aq}$ concentrations extending only to 30 μM. Unfortunately, there are no other empirical data sets from cultures yet which would allow a rigorous assessment of the possibility of change in the slope of ε_p dependence on ln

(CO_2) at higher $[CO_2]_{aq}$. Therefore, we use the 2 s.d. uncertainty of the slope of the ε_p to CO_2 calibration (0.42 is 1 s.d. for the coefficient a in Equation 5) in the Monte Carlo simulation to explores the effect of a reasonable range of variation in the slope.

Future more robust interpretations of $[CO_2]_{aq}$ from of ε_p should be supported by a realistic, experimentally validated process-based model for isotope fractionation within a multicompartment cell, an essential update to replace the original, single cell compartment, diffusive model, which is long known to not accurately simulate the processes of fractionation (Cassar et al., 2006; Hopkinson et al., 2011). Eventually, a process-based model must assimilate recent determinations of cell permeability (Blanco-Ameijeiras et al., 2020), the role of carbonic anhydrase and bicarbonate pumping (H. Zhang, Blanco-Ameijeiras, et al., 2020), and reconcile the in vitro fractionation of Rubisco (Boller et al., 2011) and other potential unidirectional reactions in carbon acquisition (Wilkes & Pearson, 2019). To date, the statistical model we have so far is the best supported tool for alkenone-based pCO_2 reconstruction in the CO_2 range of preindustrial conditions and the moderately higher pCO_2 sampled by culture data sets.

The multivariate linear regression model (Stoll et al., 2019) distinguishes the sensitivity of ε_p to CO_2 and other variables:

$$\varepsilon_p \sim a * \ln CO_2 + b * \ln light + c * \mu + d * radius \quad (5)$$

where CO_2 is the aquatic carbon dioxide concentration, light is the incident light, μ is the growth rate, and a, b, c, and d are coefficients ($a = 2.66$, $b = 2.33$, $c = -6.98$, and $d = -1.28$). To apply the multilinear regression model to calculate absolute $[CO_2]_{aq}$, cell radius, growth rate, and light need to be independently constrained. Figure S5 shows a flowchart and Table S5 an overview of the various input variables to illustrate the different steps and assumptions that go into the calculation of pCO_2. In the following sections, we review our approach to constrain cell radius, light, and growth rate.

5.2.2. Estimating Cell Radius and Light During Alkenone Production

The cell radius is taken from a semiquantitative cell size trend at Site 1088 (Figure S2) and further calculated as explained in section 3.4. Although carbonate dissolution has been observed during the LMC at Site 1088 (Diester-Haass et al., 2005), the size trend does not appear to correlate well with the amount of fragments in the sediment. One would expect an increase in fragmentation with an increase in carbonate dissolution and potentially an increase in coccolith size, since smaller coccoliths dissolve more easily. Here, the amount of fragments decreases during the LMC while the coccolith size tends to grow. It therefore seems to be safe to assume that dissolution has no major impact on the cell size trend.

The light intensity during alkenone production is difficult to estimate in the past. Photosynthetic available radiation (PAR) is a function of latitude, which has not significantly changed over time. PAR is highest at surface in the modern ocean, but it is attenuated rapidly with depth, particularly in regions with high concentrations of particles like cells in suspension in the water column. The calculation of light at depth was done using a model of penetration of PAR from surface to depth (Buiteveld, 1995; Murtugudde et al., 2002), monthly climatologies of PAR, and the diffuse attenuation coefficient for downwelling irradiance at 490 nm (Kd490). This is combined with Equation 1 in Lin et al. (2016) to calculate PAR at each depth. For Site 1088, light is assumed to be at a constant value of 25 $\mu E/m^2/s$, which corresponds to a depth during the growing season of 40–50 m. For late Pleistocene data from Site 1266, a value of 50 $\mu E/m^2/s$ is assumed, in agreement with doubled incident light at this latitude in modern-day observations (Frouin et al., 2018). Because there are few constraints on the light experienced during alkenone production, we have used values consistent with modern-day observations and maintained these constant over time. For conducting a rigorous error propagation, an error of $\pm$10% was assumed.

5.2.3. Constraints on Late Quaternary Growth Rates and Relation to ε_p

Application of the multivariate regression model requires that we estimate the absolute growth rate and assess whether it has varied over the time interval of study. Phytoplankton (including coccolithophores) growth rates (μ) in the modern ocean show dependency on SST (Sherman et al., 2016), as well as nutrient limitation, as suggested in laboratory culture data experiments (Fielding, 2013; Perrin et al., 2016). For the growth rate estimation, we use the parameterization by Krumhardt et al. (2017), which estimates growth rates based on the limitation of $[PO_4^{3-}]$ and SST:

$$\mu = \mu_{max}\left(\frac{N}{N + K_M}\right) \quad (6)$$

where N is the nutrient concentration [PO_4^{3-}], K_M the half saturation constant for that specific nutrient (K_M = 0.17 μM for [PO_4^{3-}]), and $\mu_{max} = 0.1419T^{0.8151}$ according to Fielding (2013). Temperature estimations from $U^{k'}_{37}$ are used to estimate μ_{max}.

In modern surface waters overlying the 1088 site, growth rates estimated from SST and [PO_4^{3-}] are 0.9 day^{-1}. Equatorward, in the oligotrophic waters not influenced by coastal upwelling processes such as those at Site 1266, similar growth rates of 0.9 day^{-1} are estimated, as the growth rate depression due to lower nutrient supply rates is compensated by the growth rate enhancement produced by higher temperatures (Figure 1c). As discussed in section 5.1, we propose that from the late Miocene to early Pliocene, frontal movements may have caused the waters overlying Site 1088 to experience conditions ranging between those of modern locations of Site 1088 and modern location of Site 1266. The similarity of growth rates across these settings today suggests that frontal movement need not have caused large variations in overall phytoplankton growth rates over this studies time interval.

We also derive growth rate estimates coherent with observed isotope fractionation for conditions of known late Quaternary pCO_2, an approach we term "late Quaternary anchoring." This approach provides an empirical estimation of the specific growth rate effect on ε_p in this oceanographic setting under known conditions. The purpose of this calculation is not to replicate modeled annual growth rates or [PO_4^{3-}] at this site, but rather to provide estimated growth rate and [PO_4^{3-}] which are consistent with their influence on ε_p in Equations 5 and 6, to provide more constraints on the calculation of $[CO_2]_{aq}$ from ε_p for late Miocene samples using those same equations. To this end, we use measurements of temperature and ε_p from late Quaternary glacial-interglacial pairs at Site 1266 and the more poleward location GeoB3603 (Benthien et al., 2005) close to Site 1088. First, we calculate the $[CO_2]_{aq}$ for the site predicted by equilibrium solubility given the estimated paleotemperature and ice core pCO_2 for the sampled interval. Then, we use Equations 5 and 6 to back-calculate the growth rate and [PO_4^{3-}] required so that the measured ε_p would yield a $[CO_2]_{aq}$ estimation consistent with this ice-core predicted $[CO_2]_{aq}$. For both the CO_2 solubility and the growth rate equation, we estimate temperature from $U^{k'}_{37}$. The calculated [PO_4^{3-}] ranges from 0.22 to 0.27 μM at Site 1266 and from 0.23 to 0.26 μM at GeoB3603, with lowest values during the interglacial and highest during the glacial. This examination (see Table S4) of the modern growth rate effect on ε_p suggests also that despite apparent differences in the modern annual average [PO_4^{3-}] at 10 m among these sites, there is a similar effective growth rate influence on ε_p across these sites and the [PO_4^{3-}] to attain them at these locations are similar during late Quaternary glacial-interglacials.

Alternatively, at Site 1266, we can also estimate the growth rates estimated independently from SST and proxy-derived [PO_4^{3-}] from the stratification index. We compare this result with the growth rate which satisfies the multivariate regression for the observed late Quaternary ε_p. A direct global regression between the "STRA" and the surface ocean [PO_4^{3-}] has been derived (Text S1 and Figure S4, following Hernández-Almeida et al., 2020). The stratification index values of 0.17 and 0.34 would be calculated to yield [PO_4^{3-}] values of 0.68 and 0.63 for the LGM and MIS5 samples of Site 1266, respectively, and growth rates of 1.17 and 1.31 day^{-1} given 17.5 and 20.5°C in SST. These growth rates and [PO_4^{3-}] are higher than those implied by application of the multivariate regression to observed ε_p (Table S2) as well as modern data (Figure 1). This suggests that the global "STRA" calibration overestimates the effective [PO_4^{3-}] and growth rate reflected by ε_p in this setting. This is also visualized in Figure S4 where the late Quaternary points for Site 1266 do not fall on the global regression. Therefore, an adjustment must be made to the growth rates calculated from the global "STRA"-[PO_4^{3-}] regression in order to obtain growth rates compatible with observed ε_p and Equations 5 and 6. Empirically, the "STRA"-estimated growth rates can be scaled by a factor of 0.75 to be consistent with Equations 5 and 6 and late Quaternary ice core pCO_2.

5.2.4. Estimations of Late Miocene Growth Rates and Their Variations

We evaluate multiple scenarios for the growth rate parameter when applying Equation 5 to estimate $[CO_2]_{aq}$ through the Late Miocene. In a sensitivity analysis, we evaluate scenarios where growth rate is constant, where growth rate varies depending only on proxy temperature with constant nutrients, where growth

rate varies depending on proxy-inferred [PO_4^{3-}] ranges and where growth rate varies depending on both proxy temperature and proxy-inferred [PO_4^{3-}]. The scenarios and their inputs are given in Table S3, growth rates are visualized in Figure S6, and we describe each one below.

For our first scenario, we apply Equation 6 to estimate growth rate using proxy temperature and a proxy for nutrient variations. To estimate past changes in [PO_4^{3-}], we assume that variations in [PO_4^{3-}] are inversely proportional to the stratification of the upper water column as reflected by the STRA index in our late Miocene samples (Figure S4). In Simulation 1, we assume this relationship between "STRA" and [PO_4^{3-}] is linear and apply an amplitude of [PO_4^{3-}] variations which is narrow, simulating small changes of nutrient stimulation of growth rate. This scenario would be a realistic option for the late Miocene environment at Site 1088 if the small contrast in nutrient-stimulation of growth rate observed between the modern settings of Site GeoB3603 and Site 1266 (section 5.2.3) were also representative of the evolution in nutrient-stimulation in growth rate as the Late Miocene environment at Site 1088 transitioned between more subtropical-gyre setting and a setting more proximal to the polar front. This scenario would also be a realistic option for late Miocene environment at Site 1088 if the range of variability over glacial cycles at 1266 today is representative of that observed throughout the LMC at 1088. We propose that Site 1266 is a reasonable analog to the warm, subtropical-gyre type conditions, distal from the polar fronts, which characterized the location of Site 1088 in the late Miocene. The growth rate for the LMC calculated from these [PO_4^{3-}] and the corresponding temperatures range from 0.73 to 1.12 day^{-1} (Figure 6b).

In Simulation 2, we apply the global calibration (Figure S4) to the "STRA" index measured for the late Miocene samples (Figure 5a) to estimate [PO_4^{3-}], which yields a large range in [PO_4^{3-}] of 0.39 to 0.72 μM. In calculating growth rate from these [PO_4^{3-}] estimates, we apply the scaling factor described in section 5.2.3 to account for overestimates in this calibration (Figure 6b). Modern "STRA" values near Site 1088 from the coretop calibration are around 0.2 (Figure S4), suggesting that times of lowest stratification during the LMC were similar to modern.

The trends in growth rate from Simulations 1 and 2 are similar to the trend in alkenone $C_{37:2}/C_{38:2}$ ratio (Figure 6), which has been proposed to correlate directly with the growth rate of alkenone producers based on observations in laboratory cultures (Herbert et al., 2018). Although limited calibration data exist for this proposed proxy, its trends during the LMC at Site 1088 are consistent with control by coccolithophorid growth rate. These findings are promising for the development of an additional proxy for past algal growth rates. However, further research is needed.

Simulations 3 and 4 explore the effect of growth rate variations driven uniquely by changes in [PO_4^{3-}] and not temperature, to test the degree to which the derived pCO_2 trends are independent of the modeled temperature dependence of growth rate. Therefore, temperature is held constant at 19°C which resembles the mean temperature over the LMC. Here, the estimated growth rate has a slight increasing trend after 6.5 Ma. This corresponds to the decrease in surface ocean stratification (Figure 5a) and to our approach of estimating variations in [PO_4^{3-}], which are inversely proportional to the stratification.

In Simulation 5, we employ a constant nutrient supply, since this is the most uncertain input in our calculation. Phosphate is held constant at 0.23 μM, which represents modern-day conditions at Site 1266 and we use the temperature estimated from alkenones to simulate temperature-modulation of growth rate. This produces a growth rate ranging from 0.72–0.97 day^{-1}.

Finally, Simulations 6 and 7 evaluate the sensitivity of calculated pCO_2 to the assumption of constant growth rate and constant cell size. In principle, growth rate could be invariant over time resulting from compensating effects of decreasing temperatures (μ down) and increasing nutrients (μ up) resulting from equatorward frontal movements. It is also possible that phytoplankton had adapted growth depth and season to maintain similar long-term average growth rates. The late Quaternary anchoring shows that a similar effective growth rate influences ε_p at the Sites GeoB3603 and 1266 over glacial-interglacial cycles. A constant growth rate of 0.9 day^{-1} matches these observations as well as present day surface coccolithophore growth rates during the growing season (December-January-February mean for Southern Hemisphere, Figure 1c).

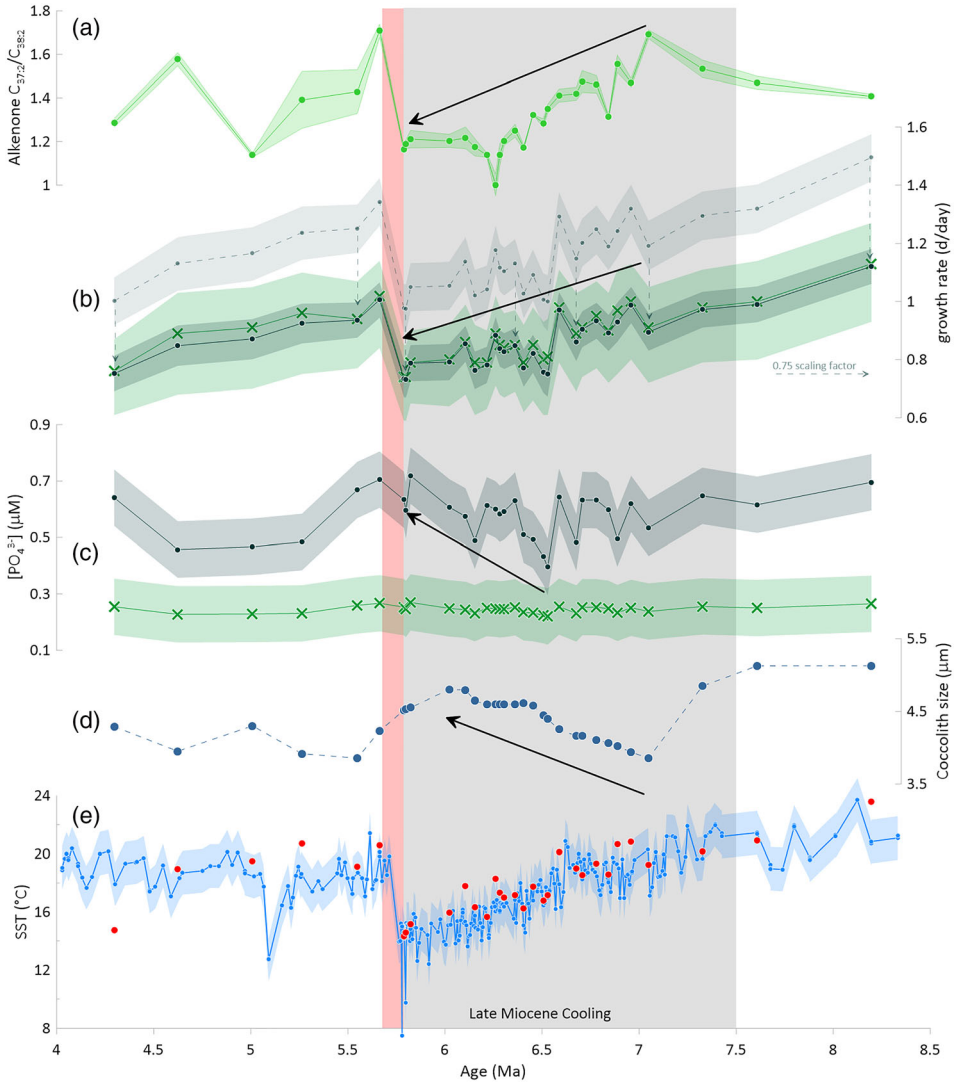

Figure 6. ODP Site 1088. (a) Ratio between alkenone compounds $C_{37:2}$ and $C_{38:2}$ with green shading showing the standard error of the mean after multiple measurements. (b) Two different temporal growth rate trends. Light green crosses (Simulation 1) are based on the narrow $[PO_4^{3-}]$. Dark green dots (Simulation 2) are based on the wide $[PO_4^{3-}]$, including a 0.75 scaling factor. The dashed line shows the actual growth rate based on the wide $[PO_4^{3-}]$ without any scaling factor. The arrows with dashed line indicate how the scaling factor reduces the value of the reported growth rate. The shading shows the 1 s.d. propagated error from the Monte Carlo simulation. (c) Light green crosses show the narrow $[PO_4^{3-}]$, and the dark green dots show the wide $[PO_4^{3-}]$ (see text for clarification). (d) Coccolith size trend. Increasing nutrient trend seems to correlate with the increase in coccolith size. (e) Alkenone-based SST from Herbert et al. (2016) in blue with a ±1.5°C error envelope. The red dots indicate the new measurements for 1088B from this study and the red shaded bar indicates the abrupt end of the LMC.

5.3. pCO_2 Estimates and Their Sensitivity to Input Parameters

5.3.1. Sensitivity of Estimated pCO_2 Change to Growth Rate Assumptions

We compare the pCO_2 estimations over the LMC from 7.6 to 5.7 Ma which result from simulations of reasonable variations in past growth rates, as well as pCO_2 resulting from further simulations serving as sensitivity analysis (as listed in Table S3). For a simplified discussion, we only comment on the rounded 50th percentile and refer the reader to the figures and supporting information for the full error estimation. As we describe, the trends in the data are more certain than the absolute past pCO_2 values.

When growth rate varies in response to both observed temperatures and varying $[PO_4^{3-}]$, according to Equation 6, based on "STRA" with a narrow range (0.22–0.27 µM), we estimate a decline in pCO_2 from

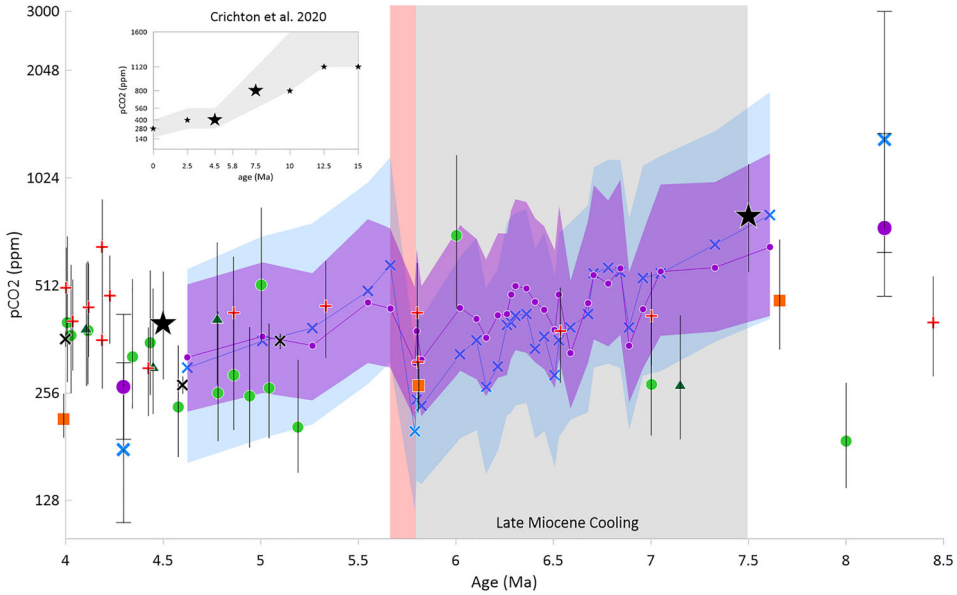

Figure 7. Available proxies for pCO_2 during the LMC. Simulation 1 with light blue crosses represents a pCO_2 trend where growth rate is calculated with the alkenone-SST proxy record and a narrow $[PO_4^{3-}]$ range from 0.22 to 0.27 μM. Simulation 6 with purple dots represents a pCO_2 trend where growth rate is kept constant at 0.9 day^{-1}. The error shading represents 1 s.d. from the Monte Carlo simulation, and it is disconnected to the youngest and oldest sample of the record because of the error bias discussed in section 5.4. Additional proxy data indicated as boron isotopes with red plus signs (Sosdian et al., 2018), dark green triangles (ODP 925) and light green dots (ODP 999) from recalculated ε_p (Stoll et al., 2019), orange squares (ODP 846) from diatom ε_p record (Mejía et al., 2017), black crosses from stomata index (Bai et al., 2015), and black stars from cGENIE modeling (Crichton et al., 2020). The red shaded bar indicates the abrupt end of the LMC and coincides with a sharp increase in atmospheric CO_2. Note the logarithmic scale of the *y* axis. Small box: long-term trend in pCO_2 from the cGENIE modeling study by Crichton et al. (2020) for a broader perspective. The two larger black stars are falling within the time period of this study.

~805 to ~200 ppm (Figure 7, Simulation 1). Simulation 2, with $[PO_4^{3-}]$ using the core top calibration and the scaling factor, yields a similar amplitude pCO_2 trend during the LMC from ~840 to ~200 ppm. We show the second simulation only in the Figure S6 since the approach has an additional uncertainty with using the scaling factor compared to Simulation 1. These two simulations additionally suggest significant sub-myr variability, which in parts of the record may reflect 400-kyr long-eccentricity cycles (Figure 8 shows cyclic minima in pCO_2 during minima in the long 400-kyr eccentricity cycle).

For Simulations 3 and 4, temperature is held constant at 19°C and growth rate varies only due to changes in $[PO_4^{3-}]$, once in a narrow and once in a broader range. In both simulations, calculated pCO_2 decreases over the LMC from ~670 to ~330 ppm. This highlights that the declining trend in pCO_2 over the LMC is not simply an artifact of temperature forcing on growth rate, as the trend exists even in simulations where growth rate is not influenced by temperature. Although there is uncertainty in the $[PO_4^{3-}]$ estimations and therefore in the absolute values of reconstructed pCO_2, the overall trend is very consistent throughout the different simulations, showing ε_p as one of the driving mechanisms behind the decreasing pCO_2 trend. In Simulation 5 with growth rate only influenced by a variable temperature, the pCO_2 trend over the LMC yields values from ~735 to ~185 ppm.

In the simulation of constant growth rates (Simulation 6, Figure 7), the calculated CO_2 decline during the LMC ranges from ~650 to ~310 ppm. A variation of this calculation (Simulation 7) assumes a constant cell size of 4.4 μm (mean size over the record) with no temporal changes; this produces only slight differences in pCO_2 and confirms that cell size is not a driving factor in the long-term pCO_2 trend derived from our records.

5.3.2. Comparison With Calculations From Diffusive Model

We compare the pCO_2 calculations made with the statistical model, with pCO_2 estimated based on the diffusive approach using "*b*," which incorporates all non-CO_2 effects on fractionation including growth rate,

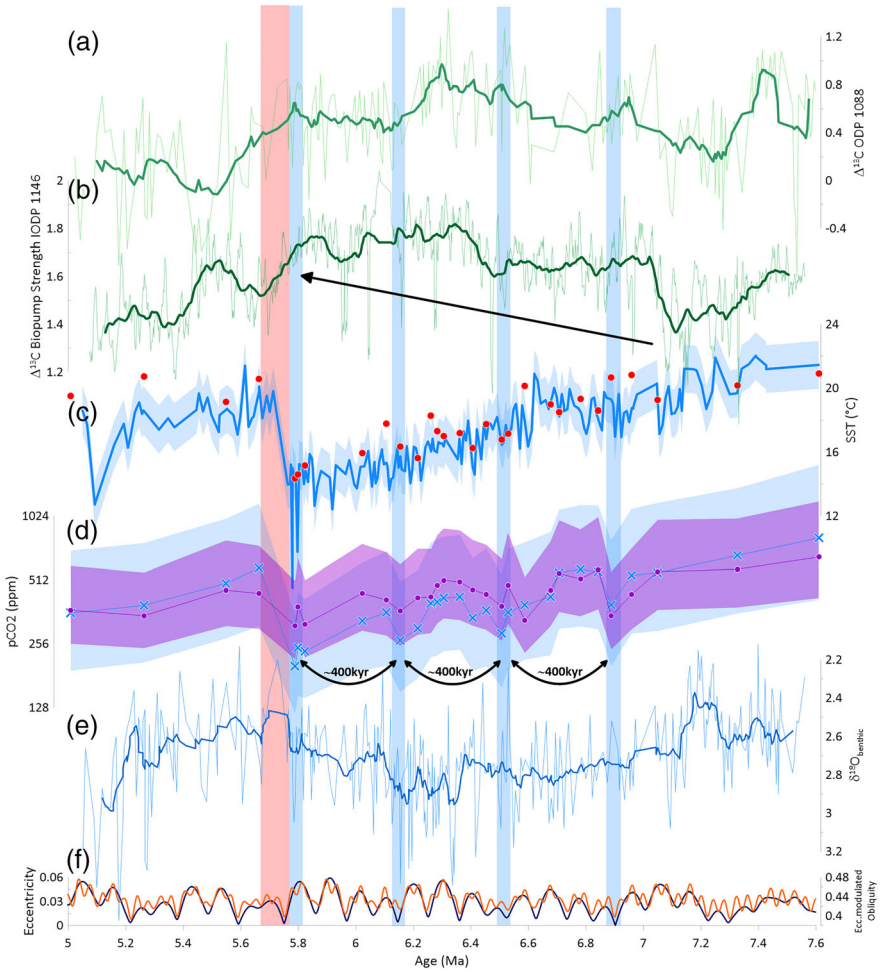

Figure 8. Subset of the record with a focus on the LMC. Note the different *x* axis. (a) $\Delta^{13}C$ between planktic (*G. bulloides*) and benthic (*Cibicidoides spp.*) foraminifera at Site 1088 in the Southern Ocean (Billups et al., 2008) with a moving average (bold) resolution of roughly 100 kyr. (b) $\Delta^{13}C$ between planktic (*G. sacculifer*) and benthic (*Cibicidoides spp.*) foraminifera at Site 1146 in the South China Sea from Holbourn et al. (2018) with a moving average (bold) resolution of roughly 100 kyr, showing a presumed strengthening of the Pacific Ocean's biological pump (black arrow). (c) Alkenone-based SST from Herbert et al. (2016) at Site 1088 with a ±1.5°C error envelope. (d) This study's pCO_2 trend over the LMC. Simulation 1 with light blue crosses and Simulation 6 with purple dots, both with 1 s.d. error shading. Indicated are distinct 400-kyr minima, occurring simultaneously with 400-kyr minima in eccentricity. (e) $\delta^{18}O_{benthic}$ from Site 1088 (Billups et al., 2008). (f) Eccentricity and obliquity cycles after Laskar et al. (2004). Blue bars show times with 400-kyr minima in pCO_2 and eccentricity, simultaneously occurring as some maximas in $\delta^{18}O_{benthic}$. The red shaded bar indicates the abrupt end of the LMC and coincides with a sharp increase in atmospheric CO_2.

cell geometry, and other physiological factors and is typically suggested to scale linearly to the phosphate concentration (Simulation 8, equation from Y. G. Zhang et al., 2013). Using the narrow range of possible $[PO_4^{3-}]$ (0.22–0.27 μM) produces the correct estimations for the glacial-interglacial values at Site 1266. However, the range of pCO_2 over the LMC with ~280 to ~215 ppm is dramatically different to all other simulations. It is not only producing constantly lower values for most of the record, the variation over the LMC with a decrease of only ~65 ppm CO_2 suggests a completely different Earth climate sensitivity (ECS) than results with the statistical model. A recently proposed variation of the diffusive "*b*" approach argues that body size is a key factor that regulates metabolic rates and that the coccolith size can be used as a proxy for growth rate, which in turn influences "*b*" (Y. G. Zhang, Henderiks, et al., 2020). We input representative salinity (has a minor effect on "*b*," we use the same value of 33.398 ± 0.5‰ as the authors) and pH (mean value of 8.05 ± 0.1 for the LMC according to the Neogene record of Sosdian et al., 2018) and our measured coccolith size (using an error of ±1 μm), alkenone temperature, and ε_p. This approach

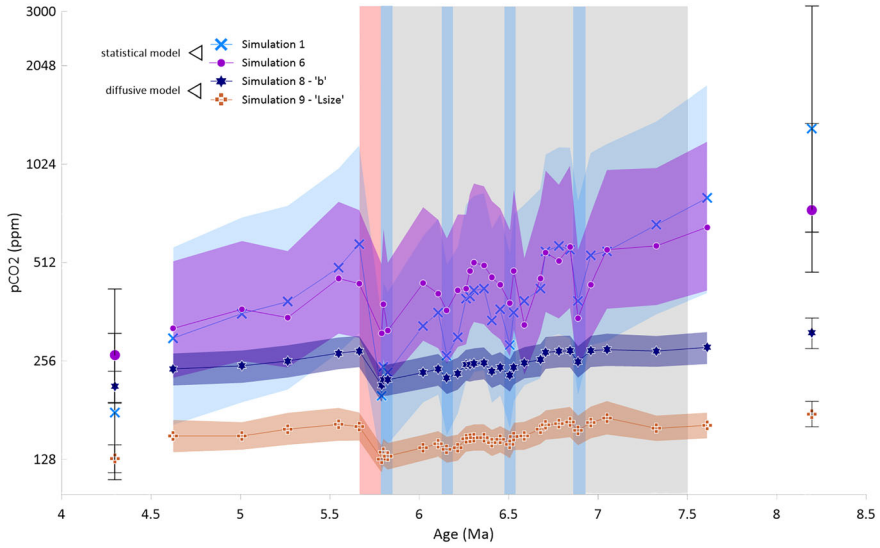

Figure 9. Alkenone-based pCO_2 reconstruction from ODP Site 1088, highlighting the contrast between the traditional, diffusive approach, and the culture-based empirical calibration. Simulations 1 and 6 show the reported trends displayed in previous figures; calculations are based on using the multilinear regression model by Stoll et al. (2019). Simulations 8 and 9 are based on the diffusive approach using the "b" term (e.g., Y. G. Zhang et al., 2013). Simulation 9 is a slight variation of it, using coccolith size (Lsize) as an indicator of growth rate and is calculated using the matlab-script by Y. G. Zhang, Henderiks, et al. (2020). Even though values and variation differ, the observed 400-kyr cycles (blue bars) are visible using both approaches.

produces again very low pCO_2 values for the Site 1088 LMC record, ranging from ~165 to ~130 ppm (Simulation 9) and showing a decrease of ~65 ppm CO_2. The stark contrast between the diffusive model and the statistical model can be seen in Figure 9.

5.4. Coherency Between Site 1088 pCO_2 Record and Other Low-Resolution pCO_2 Estimates

Based on criteria highlighted in section 5.2.4, we consider Simulations 1 and 6 to provide the pCO_2 reconstructions best supported by understanding of growth rate and late Quaternary anchoring and use them as the basis of comparisons with other pCO_2 proxy records. First, Simulation 1 represents the most dynamic resolution of growth rate where it is influenced by temporal changes in temperature and phosphate. Defining the range of possible $[PO_4^{3-}]$ with late Quaternary anchoring gives additional constraint on the absolute values. Second, Simulation 6 represents a less dynamic approach with a constant growth rate. However, this scenario could be a good alternative since it takes into account compensating effects on growth rate in a variable ocean surface environment as described in section 5.1.

The absolute values (50th percentile) we derive are similar to those provided by low-resolution pCO_2 reconstructions based on boron isotopes (Sosdian et al., 2018), plant leaves stomatal index (Bai et al., 2015), ε_p values based on a diatom record (Mejía et al., 2017), and recalculated alkenone ε_p values from tropical locations (Stoll et al., 2019) (Figure 7). The biggest discrepancy between low- and high-resolution reconstructions is for the oldest values at ~8.2 Ma, which shows the highest absolute CO_2 values reconstructed. Here, we want to emphasize one direct limitation of the statistical model, namely, that culture data upon which it is based extend only to 30 μM $[CO_2]_{aq}$. This imparts higher uncertainty in the oldest data at 1088 which exceeds the culture calibration limit. This issue can definitely be improved over time with the addition of new culture data to the statistical model. Unfortunately, we see no alternative, consistent way to calculate a value for this time period at the present time and the result we have so far is the best estimate to date. However, lower-latitude sites such as Site 925 and Site 999 remain within the range of this culture calibration throughout the last 10 Ma because of a lower CO_2 solubility and may provide more reliable absolute pCO_2 estimates prior to 7.5 Ma (Stoll et al., 2019). Even though comparison is not precise due to the absence of an orbitally resolved age model and low sampling at both sites, the estimated CO_2 values overlap within the 1 s. d. confidence interval. The youngest age point of Site 1088 (at ~4.3 Ma) also shows a much lower pCO_2

compared to other proxies. This point in our measurements is unusually cold (14.75 ± 1.5°C), compared to an adjacent sample from Herbert et al. (2016) (17.91 ± 1.5°C), and further analyses would be required to confirm if it could reflect a transient low temperature, low pCO_2 period. Additionally, the ε_p value of that sample is lower than in most other samples (Figure 4), and the reported cold temperature leads to a calculation of a low growth rate, further favoring unexpectedly low pCO_2. Our new data set provides the first high-resolution record for the time period, documenting the relationship between CO_2 decline and middle- and high-latitude cooling. We propose that our trend produced with the statistical model in its most complete form with proxy data for nutrient and cell size (Simulation 1) is the most realistic simulation derived from ε_p. This suggests a decline in atmospheric CO_2 from ~805 to ~200 ppm. Simulation 6 represents an alternative surface ocean scenario and produces a less extreme trend from ~650 to ~310 ppm. In summary, both trends record a twofold to threefold decrease in pCO_2. All of our sensitivity tests reproduce a similar decline in atmospheric CO_2, confirming that the conclusion of a late Miocene CO_2 decline is robust to uncertainties in estimations of growth rate. Finally, our reconstructed values and trend fit a recent cGENIE model (Crichton et al., 2020), that predicts CO_2 levels of 400 ppm at 4.5 Ma and 800 ppm at 7.5 Ma (Figure 7).

Estimation of the ECS for the LMC from paleodata is challenging because the LMC is best documented in middle and high latitudes, and reliable temperature data from the tropics are sparse. Temperatures poleward of 30° latitude in both hemispheres cooled by 6°C over the LMC (Herbert et al., 2016). One Mg/Ca record suggests >2°C cooling over the LMC in the South China Sea (Holbourn et al., 2018), and a second record from the tropics using planktic foraminiferal $\delta^{18}O$ also implies a 2°C cooling between 7.2 and 6.1 Ma (Drury et al., 2018) If this record is representative of the tropics, then the mean global temperature change during the LMC may have been in the order of 4°C. If the late Miocene were characterized by an ECS similar to that in climate models, 1.5–4.5°C warming per doubling of CO_2 (Solomon et al., 2007), the pCO_2 change estimated from the diffusive "*b*" model (~280 to ~215 ppm) would be accompanied by a global temperature change during the LMC of only 0.57–1.71°C, much lower than proxy temperature estimate. In contrast, given modern model ECS, the pCO_2 change estimated from application of the statistical calibration would be accompanied by a global temperature change of 3.01–9.04°C for Simulation 1 (~805 to ~200 ppm) and 1.60–4.81°C for Simulation 6 (~650 to ~310 ppm). This is well within the range of the proxy temperature estimates and shows that our favored pCO_2 estimate for the LMC is consistent with a similar ECS to that observed in models of modern climate.

5.5. Changes in the Ocean Carbon Cycle

Our high-resolution data provide new support for a decline in pCO_2 during the LMC. Previous work has observed that the LMC coincides with an intensification in the deep-water $\delta^{13}C$ gradient between the Atlantic and Pacific after the LMCIS (Hodell & Venz-Curtis, 2006; Tian et al., 2018), as well as an increase in the gradient of $\delta^{13}C$ between benthic and planktic in the South China Sea (Holbourn et al., 2018). Data at 1088 reproduce the Pacific trend of steepening in the benthic and planktic $\delta^{13}C$ gradient during the LMC (Figure 8). Additionally, we observe an increase in $C_{37}AR$ in the sediment across the LMC, whereas the opal percentage stays relatively constant (Diekmann et al., 2004). A similar increase in organic carbon flux to the seafloor is inferred from an increased benthic foraminiferal accumulate rate at this site (Diester-Haass et al., 2005). Enhanced accumulation rate of alkenones and organic carbon, potentially in the absence of evidence for increased biosilica production, may indicate increased organic preservation due to a decrease in bottom water oxygenation, characteristic of an accumulation of respired CO_2 in the deep ocean (Anderson et al., 2019). A change in ocean circulation may contribute to increased accumulation of respired carbon in the deep South Atlantic and Pacific; the ε_{Nd} decrease from −7‰ to −9.5‰ at Site 1088 also suggests an enhanced contribution of northern component waters from 7 to 5 Ma (Dausmann et al., 2017).

Thus, our confirmation of a strong pCO_2 decline is consistent with the recent hypothesis of a continuous CO_2 drawdown during the LMC due to a positive feedback loop by a strengthened biological pump (Holbourn et al., 2018). The authors argue that the strengthening of winds, due to a steeper equator to pole temperature gradient, resulted in more ocean fertilization and upwelling. These changes in the nutrient supply stimulated in turn the marine productivity which enhanced carbon storage in the deep ocean and contributed to a decline in pCO_2. In such a scenario, climate-ocean carbon cycle feedbacks analogous to those during

the LGM (e.g., Rae et al., 2018) or the mid-Pleistocene transition (MPT) (e.g., Rodríguez-Sanz et al., 2012) may have operated during the LMC. If colder, glacial climates have a stronger equator-pole temperature gradient with equatorward shifted westerlies (Herbert et al., 2016), the expansion of the Antarctic Ocean frontal system may have led to a northward expansion of sea ice cover, an enhanced stratification of the upper Southern Ocean induced by surface ocean freshening and an increased storage of respired CO_2 in the deep ocean by reducing the vertical mixing (Archer et al., 2003; Sigman et al., 2010; Stephens & Keeling, 2000; Toggweiler et al., 2006). Notably, the cooling and freshening trend is visible in our record and can be linked to the proposed shift in the frontal system. The appearance of IRDs at Site 699 and 701 (50°S) in the Southern Ocean during this time additionally supports the idea of progressively expanding sea ice (Warnke et al., 1992). Since Site 1088 is located north of the SAZ throughout the LMC, the "STRA" is not an indication of the stratification status south of the polar front (which would be more stratified due to surface freshening). However, it remains to be seen if such carbon cycle feedbacks described for the LGM or MPT can be a reasonable explanation for longer timescales such as the LMC. An unanswered question is what triggered the truncation of this feedback at 5.7 Ma.

5.6. Relationship of CO_2 to Global Climate Forcing

Previous estimates of alkenone-derived CO_2 records inferred low levels during the early to mid-Miocene with no significant shifts in the late Miocene (Pagani, Arthur, et al., 1999; Pagani, Freeman, et al., 1999). Because no long-term correlation of climate and CO_2 has been identified, Pagani et al. (2005) suggested that the late Miocene climate was decoupled from CO_2 forcing. To date, no record presented resolves CO_2 changes on an orbital timescale, and thus, the existing records may contain aliasing of orbital-scale CO_2 variability (Sosdian et al., 2018). The pCO_2 record presented in this study references the CO_2 record to temperature and sedimentological manifestations of orbital cycles. It clearly shows a coupled relationship between mid-latitude temperature and greenhouse gases. It also proposes periodic events of very low atmospheric CO_2, values (blue bars, Figure 8) that would favor Northern Hemisphere glaciation (DeConto et al., 2008).

Herbert et al. (2016) proposed that the late Miocene atmosphere descended to a critical level of CO_2, from above 500 ppm to below 350 ppm, which is considered a threshold associated with conditions that favor C4 over C3 plants. This is consistent with the here observed long-term approximately twofold to threefold decline during the latest Miocene period. Additionally, their idea that pCO_2 periodically decreased below 280 ppm is confirmed by periods in the temporal CO_2 model where very low values (<200 ppm) are reached. It has been shown that Greenland glaciation is mainly controlled by a decrease in pCO_2, while other factors, such as tectonic uplift or the closure of the Panama Seaway, play only a minor role (Lunt et al., 2008). Dominant CO_2 forcing together with the record presented here might highlight certain points in time where northern ice sheets already existed, millions of years before the intensification of Northern Hemisphere glaciation.

Findings of evidence for glaciers large enough to reach sea level, millions of years before the intensification of Northern Hemisphere glaciation have been published before. Jansen and Sjøholm (1991) found IRDs in the Norwegian Sea for a time of 5–6 Ma and John and Krissek (2002) recorded that the earliest significant ice rafting from Southeast Greenland was late Miocene (~7 Ma) in age, implying that glaciers large enough to reach sea level were present long before the onset of widespread Northern Hemisphere glaciation. Full glacial conditions in Southeast Greenland around 7 Ma were also recognized by (Larsen et al., 1994). Mercer and Sutter (1982) found glacial till deposits (roughly 4.6–7 Ma) in South America (47°S) as evidence of a local climate that was colder than today. They conclude that if global ice sheet volume at the end of the Miocene was greater than today, the excess ice would accumulate in the Northern Hemisphere. Timewise, it is suggested that the onset of widespread Northern Hemisphere glaciation is a culmination of a long-term, high-latitude cooling, starting in the late Miocene (Maslin et al., 1998).

6. Conclusions

We report the first proxy reconstruction of atmospheric pCO_2 that has a resolution high enough to show that temperature and pCO_2 are coupled during a long-term global cooling episode in the late Miocene. The absolute values of pCO_2 estimates from the ε_p proxy are always more uncertain than the trends, due to the

challenge of estimating past absolute phytoplankton growth rates. Nonetheless, the application of the revised statistical calibration, rather than the traditional diffusive equation, yields absolute pCO_2 estimates and magnitudes of pCO_2 change which are consistent with other low-resolution pCO_2 proxies and inverse model-based pCO_2 estimates. The new pCO_2 estimates suggest ECS which may have been within the range estimated by standard ocean atmosphere GCMs and do not require new physical processes to explain the observed cooling. Our work supports other findings that suggest a long phase of sea ice expansion in the Antarctic region, together with an observed frontal movement during a time of global cooling. A potential mechanism for the drawdown of CO_2 and its storage in the deep ocean is a strengthening of the biological pump together with a steepening in the equator-to-pole gradient and an expansion of the SAZ. However, further research is required to test this or other mechanisms.

Data Availability Statement

All research data are being submitted to the PANGAEA repository (https://doi.org/10.1594/PANGAEA.924529).

Acknowledgments

Sediment samples were provided by the Integrated Ocean Drilling Program (IODP). The authors thank Madallina Jaggi and Stewart Bishop from Climate Geology Group at ETH Zurich for their support and assistance in the laboratory and three anonymous reviewers whose comments greatly improved the manuscript. This research was funded by the Swiss National Science Foundation (Award 200021_182070 to Heather Stoll).

References

Anderson, R. F., Sachs, J. P., Fleisher, M. Q., Allen, K. A., Yu, J., Koutavas, A., & Jaccard, S. L. (2019). Deep-sea oxygen depletion and ocean carbon sequestration during the last ice age. *Global Biogeochemical Cycles*, *33*, 301–317. https://doi.org/10.1029/2018GB006049

Archer, D. E., Martin, P. A., Milovich, J., Brovkin, V., Plattner, G. K., & Ashendel, C. (2003). Model sensitivity in the effect of Antarctic sea ice and stratification on atmospheric pCO_2. *Paleoceanography*, *18*(1), 1012. https://doi.org/10.1029/2002PA000760

Badger, M. P., Chalk, T. B., Foster, G. L., Bown, P. R., Gibbs, S. J., Sexton, P. F., et al. (2019). Insensitivity of alkenone carbon isotopes to atmospheric CO_2 at low to moderate CO_2 levels. *Climate of the Past*, *15*, 539–554. https://doi.org/10.5194/cp-15-539-2019

Bai, Y. J., Chen, L. Q., Ranhotra, P. S., Wang, Q., Wang, Y. F., & Li, C. S. (2015). Reconstructing atmospheric CO_2 during the Plio-Pleistocene transition by fossil Typha. *Global Change Biology*, *21*, 874–881. https://doi.org/10.1111/gcb.12670

Benthien, A., Andersen, N., Schulte, S., Müller, P. J., Schneider, R. R., & Wefer, G. (2005). The carbon isotopic record of the C37: 2 alkenone in the South Atlantic: Last Glacial Maximum (LGM) vs. Holocene. *Palaeogeography, Palaeoclimatology, Palaeoecology*, *221*(1–2), 123–140. https://doi.org/10.1016/j.palaeo.2005.02.008

Billups, K. (2002). Late Miocene through early Pliocene deep water circulation and climate change viewed from the sub-Antarctic South Atlantic. *Palaeogeography, Palaeoclimatology, Palaeoecology*, *185*(3–4), 287–307. https://doi.org/10.1016/S0031-0182(02)00340-1

Billups, K., Kelly, C., & Pierce, E. (2008). The late Miocene to early Pliocene climate transition in the Southern Ocean. *Palaeogeography, Palaeoclimatology, Palaeoecology*, *267*(1–2), 31–40. https://doi.org/10.1016/j.palaeo.2008.05.013

Billups, K., & Schrag, D. (2002). Paleotemperatures and ice volume of the past 27 Myr revisited with paired Mg/Ca and $^{18}O/^{16}O$ measurements on benthic foraminifera. *Paleoceanography*, *17*(1), 184. https://doi.org/10.1029/2000PA000567

Blanco-Ameijeiras, S., Stoll, H. M., Zhang, H., & Hopkinson, B. M. (2020). Influence of temperature and CO_2 on plasma-membrane permeability to CO_2 and HCO_3^- in the marine haptophytes *Emiliania huxleyi* and *Calcidiscus leptoporus* (Prymnesiophyceae). *Journal of Phycology*, *56*, 1283–1294. https://doi.org/10.1111/jpy.13017

Boller, A. J., Thomas, P. J., Cavanaugh, C. M., & Scott, K. M. (2011). Low stable carbon isotope fractionation by coccolithophore RubisCO. *Geochimica et Cosmochimica Acta*, *75*(22), 7200–7207. https://doi.org/10.1016/j.gca.2011.08.031

Bolton, C. T., & Stoll, H. M. (2013). Late Miocene threshold response of marine algae to carbon dioxide limitation. *Nature*, *500*, 558–562. https://doi.org/10.1038/nature12448

Breitenbach, S. F., & Bernasconi, S. M. (2011). Carbon and oxygen isotope analysis of small carbonate samples (20 to 100 μg) with a GasBench II preparation device. *Rapid Communications in Mass Spectrometry*, *25*(13), 1910–1914. https://doi.org/10.1002/rcm.5052

Buiteveld, H. (1995). A model for calculation of diffuse light attenuation (PAR) and Secchi depth. *Netherlands Journal of Aquatic Ecology*, *29*(1), 55–65. https://doi.org/10.1007/BF02061789

Cassar, N., Laws, E. A., & Popp, B. N. (2006). Carbon isotopic fractionation by the marine diatom Phaeodactylum tricornutum under nutrient-and light-limited growth conditions. *Geochimica et Cosmochimica Acta*, *70*(21), 5323–5335. https://doi.org/10.1016/j.gca.2006.08.024

Cerling, T. E., Harris, J. M., MacFadden, B. J., Leakey, M. G., Quade, J., Eisenmann, V., & Ehleringer, J. R. (1997). Global vegetation change through the Miocene/Pliocene boundary. *Nature*, *389*(6647), 153–158. https://doi.org/10.1038/38229

Chase, Z., Anderson, R. F., Fleisher, M. Q., & Kubik, P. W. (2003). Accumulation of biogenic and lithogenic material in the Pacific sector of the Southern Ocean during the past 40,000 years. *Deep Sea Research Part II: Topical Studies in Oceanography*, *50*(3–4), 799–832. https://doi.org/10.1016/S0967-0645(02)00595-7

Crichton, K. A., Ridgwell, A., Lunt, D. J., Farnsworth, A., & Pearson, P. N. (2020). Data-constrained assessment of ocean circulation changes since the middle Miocene in an Earth system model. *Climate of the Past Discussions*, *2020*, 1–36.

Dausmann, V., Frank, M., Gutjahr, M., & Rickli, J. (2017). Glacial reduction of AMOC strength and long-term transition in weathering inputs into the Southern Ocean since the mid-Miocene: Evidence from radiogenic Nd and Hf isotopes. *Paleoceanography*, *32*, 265–283. https://doi.org/10.1002/2016PA003056

de Boyer Montégut, C., Madec, G., Fischer, A. S., Lazar, A., & Iudicone, D. (2004). Mixed layer depth over the global ocean: An examination of profile data and a profile-based climatology. *Journal of Geophysical Research*, *109*, C12003. https://doi.org/10.1029/2004JC002378

De Ruijter, W., Biastoch, A., Drijfhout, S., Lutjeharms, J., Matano, R., Pichevin, T., et al. (1999). Indian-Atlantic interocean exchange: Dynamics, estimation and impact. *Journal of Geophysical Research*, *104*(C9), 20,885–20,910. https://doi.org/10.1029/1998JC900099

DeConto, R. M., Pollard, D., Wilson, P. A., Pälike, H., Lear, C. H., & Pagani, M. (2008). Thresholds for Cenozoic bipolar glaciation. *Nature*, *455*(7213), 652–656. https://doi.org/10.1038/nature07337

Diekmann, B., Kuhn, G., Gersonde, R., & Mackensen, A. (2004). Middle Eocene to early Miocene environmental changes in the sub-Antarctic Southern Ocean: Evidence from biogenic and terrigenous depositional patterns at ODP Site 1090. *Global and Planetary Change*, *40*(3–4), 295–313. https://doi.org/10.1016/j.gloplacha.2003.09.001

Diester-Haass, L., Billups, K., & Emeis, K. C. (2005). In search of the late Miocene–early Pliocene "biogenic bloom" in the Atlantic Ocean (Ocean Drilling Program Sites 982, 925, and 1088). *Paleoceanography*, *20*, PA4001. https://doi.org/10.1029/2005PA001139

Drury, A. J., John, C. M., & Shevenell, A. E. (2016). Evaluating climatic response to external radiative forcing during the late Miocene to early Pliocene: New perspectives from eastern equatorial Pacific (IODP U1338) and North Atlantic (ODP 982) locations. *Paleoceanography*, *31*, 167–184. https://doi.org/10.1002/2015PA002881

Drury, A. J., Lee, G., Gray, W. R., Lyle, M., Westerhold, T., Shevenell, A. E., & John, C. M. (2018). Deciphering the state of the late Miocene to early Pliocene equatorial Pacific. *Paleoceanography and Paleoclimatology*, *33*, 246–263. https://doi.org/10.1002/2017PA003245

Drury, A. J., Westerhold, T., Frederichs, T., Tian, J., Wilkens, R., Channell, J. E., et al. (2017). Late Miocene climate and time scale reconciliation: Accurate orbital calibration from a deep-sea perspective. *Earth and Planetary Science Letters*, *475*, 254–266. https://doi.org/10.1016/j.epsl.2017.07.038

Elderfield, H., Vautravers, M., & Cooper, M. (2002). The relationship between shell size and Mg/Ca, Sr/Ca, $\delta^{18}O$, and $\delta^{13}C$ of species of planktonic foraminifera. *Geochemistry, Geophysics, Geosystems*, *3*(8), 1052. https://doi.org/10.1029/2001GC000194

Fielding, S. R. (2013). Emiliania huxleyi specific growth rate dependence on temperature. *Limnology and Oceanography*, *58*, 663–666. https://doi.org/10.4319/lo.2013.58.2.0663

Freeman, K. H., & Hayes, J. (1992). Fractionation of carbon isotopes by phytoplankton and estimates of ancient CO_2 levels. *Global Biogeochemical Cycles*, *6*(2), 185–198. https://doi.org/10.1029/92GB00190

Frouin, R., Ramon, D., Boss, E., Jolivet, D., Compiègne, M., Tan, J., et al. (2018). Satellite radiation products for ocean biology and biogeochemistry: Needs, state-of-the-art, gaps, development priorities, and opportunities. *Frontiers in Marine Science*, *5*, 3. https://doi.org/10.3389/fmars.2018.00003

Fuertes, M.-Á., Flores, J.-A., & Sierro, F. J. (2014). The use of circularly polarized light for biometry, identification and estimation of mass of coccoliths. *Marine Micropaleontology*, *113*, 44–55. https://doi.org/10.1016/j.marmicro.2014.08.007

Garcia, H. E., Locarnini, R. A., Boyer, T. P., Antonov, J. I., Baranova, O. K., Zweng, M. M., et al. (2013). World Ocean Atlas 2013. Vol. 4: Dissolved inorganic nutrients (phosphate, nitrate, silicate). In S. Levitus & A. Mishonov (Eds.), *NOAA Atlas NESDIS 76* (25 pp.).

Gersonde, R., Abelmann, A., Brathauer, U., Becquey, S., Bianchi, C., Cortese, G., et al. (2003). Last glacial sea surface temperatures and sea-ice extent in the Southern Ocean (Atlantic-Indian sector): A multiproxy approach. *Paleoceanography*, *18*(3), 1061. https://doi.org/10.1029/2002PA000809

Gersonde, R., Hodell, D. A., & Blum, P. (1999). Leg 177 summary: Southern ocean paleoceanography. Paper presented at the Proc. Ocean Drill. Program Initial Rep.

Guitián, J., Dunkley Jones, T., Hernández-Almeida, I., Löffel, T., & Stoll, H. M. (2020). Adaptations of coccolithophore size to selective pressures during the Oligocene - Early Miocene high CO_2 world. *Paleoceanography and Paleoclimatology*, *35*, e2020PA003918. https://doi.org/10.1029/2020PA003918

Henderiks, J., & Pagani, M. (2007). Refining ancient carbon dioxide estimates: Significance of coccolithophore cell size for alkenone-based pCO_2 records. *Paleoceanography*, *22*, PA3202. https://doi.org/10.1029/2006PA001399

Herbert, T., George, S. E., Marino, M., Maiorano, P., & Thunell, R. (2018). Alkenone-based approaches to productivity and growth rate. Paper presented at the AGU Fall Meeting Abstracts.

Herbert, T., Lawrence, K. T., Tzanova, A., Peterson, L. C., Caballero-Gill, R., & Kelly, C. S. (2016). Late Miocene global cooling and the rise of modern ecosystems. *Nature Geoscience*, *9*, 843–847. https://doi.org/10.1038/ngeo2813

Hernández-Almeida, I., Krumhardt, K., Zhang, H., & Stoll, H. (2020). Estimation of physiological factors controlling carbon isotope fractionation in coccolithophores in photic zone and core-top samples. *Geochemistry, Geophysics, Geosystems*, *21*, e2020GC009272. https://doi.org/10.1029/2020GC009272

Hilgen, F., Lourens, L., Van Dam, J., Beu, A., Boyes, A., Cooper, R., et al. (2012). The Neogen period. In *The geologic time scale Volume* (Vol. 2, pp. 923–978). Boston: Elsevier.

Hodell, D. A., Charles, C. D., Curtis, J. H., Mortyn, P. G., Ninnemann, U. S., & Venz, K. A. (2003). *Data report: Oxygen isotope stratigraphy of ODP Leg 177 Sites 1088, 1089, 1090, 1093, and 1094*. Paper presented at the Proc. Ocean Drill. Program Sci. Results, 177, 1–26. Retrieved from http://www-odp.tamu.edu/publications/177_SR/volume/chapters/SR177_09.pdf

Hodell, D. A., Curtis, J. H., Sierro, F. J., & Raymo, M. E. (2001). Correlation of late Miocene to early Pliocene sequences between the Mediterranean and North Atlantic. *Paleoceanography*, *16*(2), 164–178. https://doi.org/10.1029/1999PA000487

Hodell, D. A., & Venz-Curtis, K. A. (2006). Late Neogene history of deepwater ventilation in the Southern Ocean. *Geochemistry, Geophysics, Geosystems*, *7*, Q09001. https://doi.org/10.1029/2005GC001211

Holbourn, A. E., Kuhnt, W., Clemens, S. C., Kochhann, K. G., Jöhnck, J., Lübbers, J., & Andersen, N. (2018). Late Miocene climate cooling and intensification of southeast Asian winter monsoon. *Nature Communications*, *9*, 1–13. https://doi.org/10.1038/s41467-018-03950-1

Hopkins, J., Henson, S. A., Painter, S. C., Tyrrell, T., & Poulton, A. J. (2015). Phenological characteristics of global coccolithophore blooms. *Global Biogeochemical Cycles*, *29*, 239–253. https://doi.org/10.1002/2014GB004919

Hopkinson, B. M., Dupont, C. L., Allen, A. E., & Morel, F. M. (2011). Efficiency of the CO_2-concentrating mechanism of diatoms. *Proceedings of the National Academy of Sciences*, *108*(10), 3830–3837. https://doi.org/10.1073/pnas.1018062108

Jansen, E., & Sjøholm, J. (1991). Reconstruction of glaciation over the past 6 Myr from ice-borne deposits in the Norwegian Sea. *Nature*, *349*(6310), 600–603. https://doi.org/10.1038/349600a0

Jasper, J. P., Hayes, J., Mix, A. C., & Prahl, F. G. (1994). Photosynthetic fractionation of ^{13}C and concentrations of dissolved CO_2 in the central equatorial Pacific during the last 255,000 years. *Paleoceanography*, *9*(6), 781–798. https://doi.org/10.1029/94PA02116

John, K. E. S., & Krissek, L. A. (2002). The late Miocene to Pleistocene ice-rafting history of southeast Greenland. *Boreas*, *31*(1), 28–35. https://doi.org/10.1080/03009480210651

Jonkers, L., van Heuven, S., Zahn, R., & Peeters, F. J. (2013). Seasonal patterns of shell flux, $\delta^{18}O$ and $\delta^{13}C$ of small and large *N. pachyderma* (s) and *G. bulloides* in the subpolar North Atlantic. *Paleoceanography*, *28*, 164–174. https://doi.org/10.1002/palo.20018

Keller, G. (1985). Depth stratification of planktonic foraminifers in the Miocene ocean. *The Miocene ocean: Paleoceanography and biogeography*, *163*, 177–196.

Kemp, A., Grigorov, I., Pearce, R. B., & Garabato, A. N. (2010). Migration of the Antarctic Polar Front through the mid-Pleistocene transition: Evidence and climatic implications. *Quaternary Science Reviews*, *29*(17–18), 1993–2009. https://doi.org/10.1016/j.quascirev.2010.04.027

Kennett, J. P., Keller, G., Srinivasan, M. S., & Kennett, J. P. (1985). Miocene planktonic foraminiferal biogeography and paleoceanographic development of the Indo-Pacific region. In *The Miocene ocean: Paleoceanography and biogeography* (pp. 197–236). Boulder, Colorado: Geological Society of America.

Kohfeld, K., Graham, R., De Boer, A., Sime, L., Wolff, E., Le Quéré, C., & Bopp, L. (2013). Southern Hemisphere westerly wind changes during the Last Glacial Maximum: Paleo-data synthesis. *Quaternary Science Reviews*, *68*, 76–95. https://doi.org/10.1016/j.quascirev.2013.01.017

Krumhardt, K. M., Lovenduski, N. S., Iglesias-Rodriguez, M. D., & Kleypas, J. A. (2017). Coccolithophore growth and calcification in a changing ocean. *Progress in Oceanography*, *159*, 276–295. https://doi.org/10.1016/j.pocean.2017.10.007

Kucera, M. (2007). Chapter six planktonic foraminifera as tracers of past oceanic environments. *Developments in Marine Geology*, *1*, 213–262. https://doi.org/10.1016/S1572-5480(07)01011-1

LaRiviere, J. P., Ravelo, A. C., Crimmins, A., Dekens, P. S., Ford, H. L., Lyle, M., & Wara, M. W. (2012). Late Miocene decoupling of oceanic warmth and atmospheric carbon dioxide forcing. *Nature*, *486*(7401), 97–100. https://doi.org/10.1038/nature11200

Larsen, H., Saunders, A., Clift, P., Beget, J., Wei, W., & Spezzaferri, S. (1994). Seven million years of glaciation in Greenland. *Science*, *264*(5161), 952–955. https://doi.org/10.1126/science.264.5161.952

Laskar, J., Robutel, P., Joutel, F., Gastineau, M., Correia, A., & Levrard, B. (2004). A long-term numerical solution for the insolation quantities of the Earth. *Astronomy & Astrophysics*, *428*(1), 261–285. https://doi.org/10.1051/0004-6361:20041335

LeGrande, A. N., & Schmidt, G. A. (2006). Global gridded data set of the oxygen isotopic composition in seawater. *Geophysical Research Letters*, *33*, L12604. https://doi.org/10.1029/2006GL026011

Lin, J., Lee, Z., Ondrusek, M., & Du, K. (2016). Remote sensing of normalized diffuse attenuation coefficient of downwelling irradiance. *Journal of Geophysical Research: Oceans*, *121*, 6717–6730. https://doi.org/10.1002/2016JC011895

Locarnini, R. A., Mishonov, A. V., Antonov, J. I., Boyer, T. P., Garcia, H. E., Baranova, O. K., et al. (2013). World ocean atlas 2013. Volume 1, Temperature.

Lunt, D. J., Foster, G. L., Haywood, A. M., & Stone, E. J. (2008). Late Pliocene Greenland glaciation controlled by a decline in atmospheric CO_2 levels. *Nature*, *454*(7208), 1102–1105. https://doi.org/10.1038/nature07223

Marino, M., & Flores, J. A. (2002). Miocene to Pliocene calcareous nannofossil biostratigraphy at ODP Leg 177 Sites 1088 and 1090. *Marine Micropaleontology*, *45*(3–4), 291–307. https://doi.org/10.1016/S0377-8398(02)00033-6

Martínez-Garcia, A., Rosell-Melé, A., McClymont, E. L., Gersonde, R., & Haug, G. H. (2010). Subpolar link to the emergence of the modern equatorial Pacific cold tongue. *Science*, *328*(5985), 1550–1553. https://doi.org/10.1126/science.1184480

Maslin, M., Li, X., Loutre, M.-F., & Berger, A. (1998). The contribution of orbital forcing to the progressive intensification of Northern Hemisphere glaciation. *Quaternary Science Reviews*, *17*(4–5), 411–426. https://doi.org/10.1016/S0277-3791(97)00047-4

Matthews, R., Curry, W., Lohmann, K., Sommer, M., & Poore, R. (1980). Late Miocene palaeo-oceanography of the Atlantic: Oxygen isotope data on planktonic and benthic Foraminifera. *Nature*, *283*(5747), 555–557. https://doi.org/10.1038/283555a0

Mejía, L. M., Méndez-Vicente, A., Abrevaya, L., Lawrence, K. T., Ladlow, C., Bolton, C., et al. (2017). A diatom record of CO_2 decline since the late Miocene. *Earth and Planetary Science Letters*, *479*, 18–33. https://doi.org/10.1016/j.epsl.2017.08.034

Mercer, J. H., & Sutter, J. F. (1982). Late Miocene–earliest Pliocene glaciation in southern Argentina: Implications for global ice-sheet history. *Palaeogeography, Palaeoclimatology, Palaeoecology*, *38*(3–4), 185–206. https://doi.org/10.1016/0031-0182(82)90003-7

Miller, K. G., Kominz, M. A., Browning, J. V., Wright, J. D., Mountain, G. S., Katz, M. E., et al. (2005). The Phanerozoic record of global sea-level change. *Science*, *310*(5752), 1293–1298. https://doi.org/10.1126/science.1116412

Mook, W., Bommerson, J., & Staverman, W. (1974). Carbon isotope fractionation between dissolved bicarbonate and gaseous carbon dioxide. *Earth and Planetary Science Letters*, *22*(2), 169–176. https://doi.org/10.1016/0012-821X(74)90078-8

Müller, P. J., Kirst, G., Ruhland, G., Von Storch, I., & Rosell-Melé, A. (1998). Calibration of the alkenone paleotemperature index U37K′ based on core-tops from the eastern South Atlantic and the global ocean (60°N–60°S). *Geochimica et Cosmochimica Acta*, *62*(10), 1757–1772. https://doi.org/10.1016/S0016-7037(98)00097-0

Murtugudde, R., Beauchamp, J., McClain, C. R., Lewis, M., & Busalacchi, A. J. (2002). Effects of penetrative radiation on the upper tropical ocean circulation. *Journal of Climate*, *15*(5), 470–486. https://doi.org/10.1175/1520-0442(2002)015<0470:EOPROT>2.0.CO;2

Norris, R., Corfield, R., & Cartlidge, J. (1994). Evolutionary ecology of *Globorotalia (Globoconella)* (planktic foraminifera). *Marine Micropaleontology*, *23*(2), 121–145. https://doi.org/10.1016/0377-8398(94)90004-3

Pagani, M. (2014). Biomarker-based inferences of past climate: The alkenone pCO_2 proxy. In H. D. Holland & K. K. Turekian (Eds.), *Treatise on Geochemistry*. (pp. 361–378). Oxford: Elsevier.

Pagani, M., Arthur, M. A., & Freeman, K. H. (1999). Miocene evolution of atmospheric carbon dioxide. *Paleoceanography*, *14*(3), 273–292. https://doi.org/10.1029/1999PA900006

Pagani, M., Freeman, K. H., & Arthur, M. A. (1999). Late Miocene atmospheric CO_2 concentrations and the expansion of C4 grasses. *Science*, *285*(5429), 876–879. https://doi.org/10.1126/science.285.5429.876

Pagani, M., Zachos, J. C., Freeman, K. H., Tipple, B., & Bohaty, S. (2005). Marked decline in atmospheric carbon dioxide concentrations during the Paleogene. *Science*, *309*(5734), 600–603. https://doi.org/10.1126/science.1110063

Paulsen, H. (2005). Miocene changes in the vertical structure of the Southeast Atlantic near-surface water column: Influence on the paleoproductivity. Dissertation thesis, 93 pp, Univ. Bremen, Germany,

Perrin, L., Probert, I., Langer, G., & Aloisi, G. (2016). Growth of the coccolithophore Emiliania huxleyi in light-and nutrient-limited batch reactors: Relevance for the BIOSOPE deep ecological niche of coccolithophores. *Biogeosciences*, *13*, 5983–6001. https://doi.org/10.5194/bg-13-5983-2016

Popp, B. N., Kenig, F., Wakeham, S. G., Laws, E. A., & Bidigare, R. R. (1998). Does growth rate affect ketone unsaturation and intracellular carbon isotopic variability in Emiliania huxleyi? *Paleoceanography*, *13*(1), 35–41. https://doi.org/10.1029/97PA02594

Prasanna, K., Ghosh, P., Bhattacharya, S., Mohan, K., & Anilkumar, N. (2016). Isotopic disequilibrium in *Globigerina bulloides* and carbon isotope response to productivity increase in Southern Ocean. *Scientific Reports*, *6*, 21533. https://doi.org/10.1038/srep21533

Rae, J. W., Burke, A., Robinson, L., Adkins, J., Chen, T., Cole, C., et al. (2018). CO_2 storage and release in the deep Southern Ocean on millennial to centennial timescales. *Nature*, *562*, 569–573. https://doi.org/10.1038/s41586-018-0614-0

Rau, G. H., Riebesell, U., & Wolf-Gladrow, D. (1996). A model of photosynthetic ^{13}C fractionation by marine phytoplankton based on diffusive molecular CO_2 uptake. *Marine Ecology Progress Series*, *133*, 275–285. https://doi.org/10.3354/meps133275

Ravelo, A. C., & Hillaire-Marcel, C. (2007). Chapter eighteen the use of oxygen and carbon isotopes of foraminifera in paleoceanography. *Developments in Marine Geology*, *1*, 735–764. https://doi.org/10.1016/S1572-5480(07)01023-8

Rodríguez-Sanz, L., Mortyn, P. G., Martínez-Garcia, A., Rosell-Melé, A., & Hall, I. R. (2012). Glacial Southern Ocean freshening at the onset of the Middle Pleistocene climate transition. *Earth and Planetary Science Letters*, *345*, 194–202. https://doi.org/10.1016/j.epsl.2012.06.016

Schuster, M., Duringer, P., Ghienne, J.-F., Vignaud, P., Mackaye, H. T., Likius, A., & Brunet, M. (2006). The age of the Sahara desert. *Science*, *311*(5762), 821–821. https://doi.org/10.1126/science.1120161

Shackleton, N. (1974). Attainment of isotopic equilibrium between ocean water and the benthonic foraminifera genus Uvigerina: Isotopic changes in the ocean during the last glacial.

Shackleton, N., & Hall, M. (1997). 24. The late Miocene stable isotope record, Site 926. Paper presented at the Proceedings of the Ocean Drilling Program, Sci. Results.

Sherman, E., Moore, J. K., Primeau, F., & Tanouye, D. (2016). Temperature influence on phytoplankton community growth rates. *Global Biogeochemical Cycles*, *30*, 550–559. https://doi.org/10.1002/2015GB005272

Sigman, D. M., Hain, M. P., & Haug, G. H. (2010). The polar ocean and glacial cycles in atmospheric CO_2 concentration. *Nature*, *466*(7302), 47–55. https://doi.org/10.1038/nature09149

Solomon, S., Manning, M., Marquis, M., & Qin, D. (2007). *Climate change 2007—The physical science basis: Working group I contribution to the fourth assessment report of the IPCC* (Vol. 4). Cambridge, UK and New York, NY: Cambridge University Press.

Sosdian, S. M., Greenop, R., Hain, M., Foster, G. L., Pearson, P. N., & Lear, C. H. (2018). Constraining the evolution of Neogene ocean carbonate chemistry using the boron isotope pH proxy. *Earth and Planetary Science Letters*, *498*, 362–376. https://doi.org/10.1016/j.epsl.2018.06.017

Stephens, B. B., & Keeling, R. F. (2000). The influence of Antarctic sea ice on glacial-interglacial CO_2 variations. *Nature*, *404*(6774), 171–174. https://doi.org/10.1038/35004556

Stoll, H. M., Guitian, J., Hernandez-Almeida, I., Mejia, L. M., Phelps, S., Polissar, P., et al. (2019). Upregulation of phytoplankton carbon concentrating mechanisms during low CO_2 glacial periods and implications for the phytoplankton pCO_2 proxy. *Quaternary Science Reviews*, *208*, 1–20. https://doi.org/10.1016/j.quascirev.2019.01.012

Tian, J., Ma, X., Zhou, J., Jiang, X., Lyle, M., Shackford, J., & Wilkens, R. (2018). Paleoceanography of the east equatorial Pacific over the past 16 Myr and Pacific–Atlantic comparison: High resolution benthic foraminiferal $\delta^{18}O$ and $\delta^{13}C$ records at IODP Site U1337. *Earth and Planetary Science Letters*, *499*, 185–196. https://doi.org/10.1016/j.epsl.2018.07.025

Toggweiler, J. R., Russell, J. L., & Carson, S. R. (2006). Midlatitude westerlies, atmospheric CO_2, and climate change during the ice ages. *Paleoceanography*, *21*, PA2005. https://doi.org/10.1029/2005PA001154

Valdes, P. J., Armstrong, E., Badger, M. P., Bradshaw, C. D., Bragg, F., Davies-Barnard, T., et al. (2017). The BRIDGE HadCM3 family of climate models: HadCM3@ Bristol v1. 0. *Geoscientific Model Development*, *10*, 3715–3743. https://doi.org/10.5194/gmd-10-3715-2017

Warnke, D. A., Allen, C. P., Muller, D. W., Hodell, D. A., & Brunner, C. A. (1992). Miocene-Pliocene Antarctic glacial evolution: A synthesis of ice-rafted debris, stable isotope, and planktonic foraminiferal indicators, ODP Leg 114. *The Antarctic Paleoenvironment: A Perspective on Global Change: Part One*, *56*, 311–326. https://doi.org/10.1029/AR056p0311

Wilkens, R. H., Westerhold, T., Drury, A. J., Lyle, M., Gorgas, T., & Tian, J. (2017). Revisiting the Ceara Rise, equatorial Atlantic Ocean: Isotope stratigraphy of ODP Leg 154 from 0 to 5 Ma. *Climate of the Past*, *13*, 779–793. https://doi.org/10.5194/cp-13-779-2017

Wilkes, E. B., & Pearson, A. (2019). A general model for carbon isotopes in red-lineage phytoplankton: Interplay between unidirectional processes and fractionation by RubisCO. *Geochimica et Cosmochimica Acta*, *265*, 163–181. https://doi.org/10.1016/j.gca.2019.08.043

Zachos, J., Kroon, D., Bloom, P., & Party, S. (2004). Site 1266. Paper presented at the Proceedings of the Ocean Drilling Program, Initial Reports.

Zachos, J., Pagani, M., Sloan, L., Thomas, E., & Billups, K. (2001). Trends, rhythms, and aberrations in global climate 65 Ma to present. *Science*, *292*(5517), 686–693. https://doi.org/10.1126/science.1059412

Zhang, H., Blanco-Ameijeiras, S., Hopkins, B. M., Bernasconi, S. M., Mejia, L. M., Liu, C., & Stoll, H. (2020). An isotope label method for empirical detection of carbonic anhydrase in the calcification pathway of the coccolithophore *Emiliania huxleyi*. *Geochimica et Cosmochimica Acta*, *292*, 78–93. https://doi.org/10.1016/j.gca.2020.09.008

Zhang, Y. G., Henderiks, J., & Liu, X. (2020). Refining the alkenone-pCO_2 method II: Towards resolving the physiological parameter '*b*'. *Geochimica et Cosmochimica Acta*, *281*, 118–134. https://doi.org/10.1016/j.gca.2020.05.002

Zhang, Y. G., Pagani, M., Liu, Z., Bohaty, S. M., & DeConto, R. (2013). A 40-million-year history of atmospheric CO_2. *Philosophical Transactions of the Royal Society A: Mathematical. Physical and Engineering Sciences*, *371*, 20130096. https://doi.org/10.1098/rsta.2013.0096